CANCER

Temporal regulation of acetylation status determines PARP1 role in DNA damage response and metabolic homeostasis

Witty Tyagi and Sanjeev Das*

Copyright © 2024 The Authors, some rights reserved; exclusive licensee American Association for the Advancement of Science. No claim to original U.S. Government Works. Distributed under a Creative Commons Attribution NonCommercial License 4.0 (CC BY-NC).

Poly(ADP-ribose) polymerase 1 (PARP1) is an abundant nuclear protein involved in DNA repair, chromatin structure, and transcription. However, the regulation of its different functions remains poorly understood. Here, we report the role of PARP1 acetylation status in modulating its DNA repair and transactivation functions. We demonstrate that histone deacetylase 5 (HDAC5) determines PARP1 acetylation at Lys498 and Lys521 sites. HDAC5-mediated deacetylation at Lys498 site regulates PARP1 DNA damage response and facilitates efficient recruitment of DNA repair factors at damaged sites, thereby promoting cell survival. Additionally, HDAC5-mediated deacetylation at Lys521 site promotes PARP1 coactivator function, resulting in induction of proliferative and metabolic genes in an activating transcription factor 4-dependent manner. Thus, PARP1 induces metabolic adaptation to spur malignant phenotype. Our studies in mouse tumor models suggest that pharmacological inhibition of PARP1 enzymatic activity does not block tumor progression robustly as transactivation function remains unperturbed. These findings provide key mechanistic insights into PARP1 regulation and expand its role in tumor development.

INTRODUCTION

Poly(ADP-ribose) polymerase 1 (PARP1) is a cellular stress responder and among the first signaling proteins being recruited to both single-stranded breaks and double-stranded breaks (*1*). The catalytic function of PARP1 is activated in response to genotoxic stress by attaching a negatively charged polymer termed poly(ADP-ribose) (PAR) to itself and other protein targets (*2*). Poly-ADP-ribosylation (PARylation) facilitates the recruitment of DNA repair proteins, including XRCC1, MREII, RAD51, and histone-modifying enzymes to DNA lesions (*3*). In addition to its role as a DNA damage responder, PARP1 acts as a potent modulator of gene transcription which may not necessarily require its enzymatic activity (*4*). The transcriptional regulatory functions of PARP1 encompass enhancer binding, association with insulators, modulation of chromatin structure, and direct regulation of transcription factors. PARP1-mediated transcriptional regulation plays a key role in human malignancies, including colorectal, breast, and gastric cancers (*5*). However, the dynamic regulation of its DNA repair and transactivation functions is poorly understood.

Histone deacetylase 5 (HDAC5) is a histone deacetylase belonging to the highly conserved class IIa family of Zn^{2+}-dependent histone deacetylases. HDAC5 is predominantly regulated by post-translational modifications, which determine its subcellular localization. Ca^{2+}/calmodulin-dependent protein kinase has been reported to phosphorylate HDAC5, which promotes its binding with 14-3-3, resulting in cytoplasmic retention (*6*). On the other hand, cAMP-dependent protein kinase A phosphorylates HDAC5 to disrupt its interaction with 14-3-3, which promotes nuclear accumulation of HDAC5 (*7*). At the posttranscriptional level, a few microRNAs have also been reported to regulate HDAC5 expression. miR-2861 has been observed to repress HDAC5 expression to promote osteoblast differentiation (*8*). HDAC5 not only catalyzes the deacetylation of nuclear histones but also deacetylates or forms complexes with other proteins to modulate oncogenic signaling pathways (*9*). Consequently, HDAC5 plays a prominent role in tumor cell proliferation (*10*), metastasis (*11*), and metabolism (*12*). Aberrant expression of HDAC5 has also been reported in diverse cancers, including breast, lung, and colorectal cancer (*13*). Hence, exploring its substrate repertoire can enhance our understanding of its role in altered gene expression during tumorigenesis.

In this study, we sought to investigate the role of PARP1 acetylation status in modulating its DNA repair and transactivation functions. Using a biochemical approach, we established HDAC5 as the bona fide deacetylase that determines PARP1 acetylation. HDAC5-mediated deacetylation at the Lys^{498} site is critical for PARP1-dependent DNA damage response by promoting PARylation, thereby preventing chromatin trapping and triggering the recruitment of repair factors. Moreover, HDAC5 also deacetylates PARP1 at Lys^{521}, which modulates its transactivation function, thereby inducing metabolic reprogramming under genotoxic stress conditions. Thus, our study sheds light on the intricate regulatory mechanisms that determine the impact of PARP1 acetylation status on DNA damage response and metabolic adaptation.

RESULTS

PARP1 interacts with HDAC5

To understand the molecular axis and determine the precise role of HDAC5 under genotoxic stress conditions, we analyzed the acetylome upon HDAC5 depletion (Fig. 1A). Our analysis revealed increased acetylation of various proteins, prominent among which was PARP1. To determine whether PARP1 is a bona fide HDAC5 substrate, we first performed coimmunoprecipitation experiments. Our data suggest that HDAC5 coimmunoprecipitated with PARP1 (Fig. 1B, left). Concurring results were obtained upon reverse coimmunoprecipitation (Fig. 1B, right). Direct interaction between PARP1 and HDAC5 was also confirmed by performing glutathione *S*-transferase (GST) pull-down experiments using bacterially expressed and purified proteins (Fig. 1C and fig. S1A). We next examined the interaction between PARP1 and HDAC5 under genotoxic

Molecular Oncology Laboratory, National Institute of Immunology, Aruna Asaf Ali Marg, New Delhi-110067, India.
*Corresponding author. Email: sdas@nii.ac.in

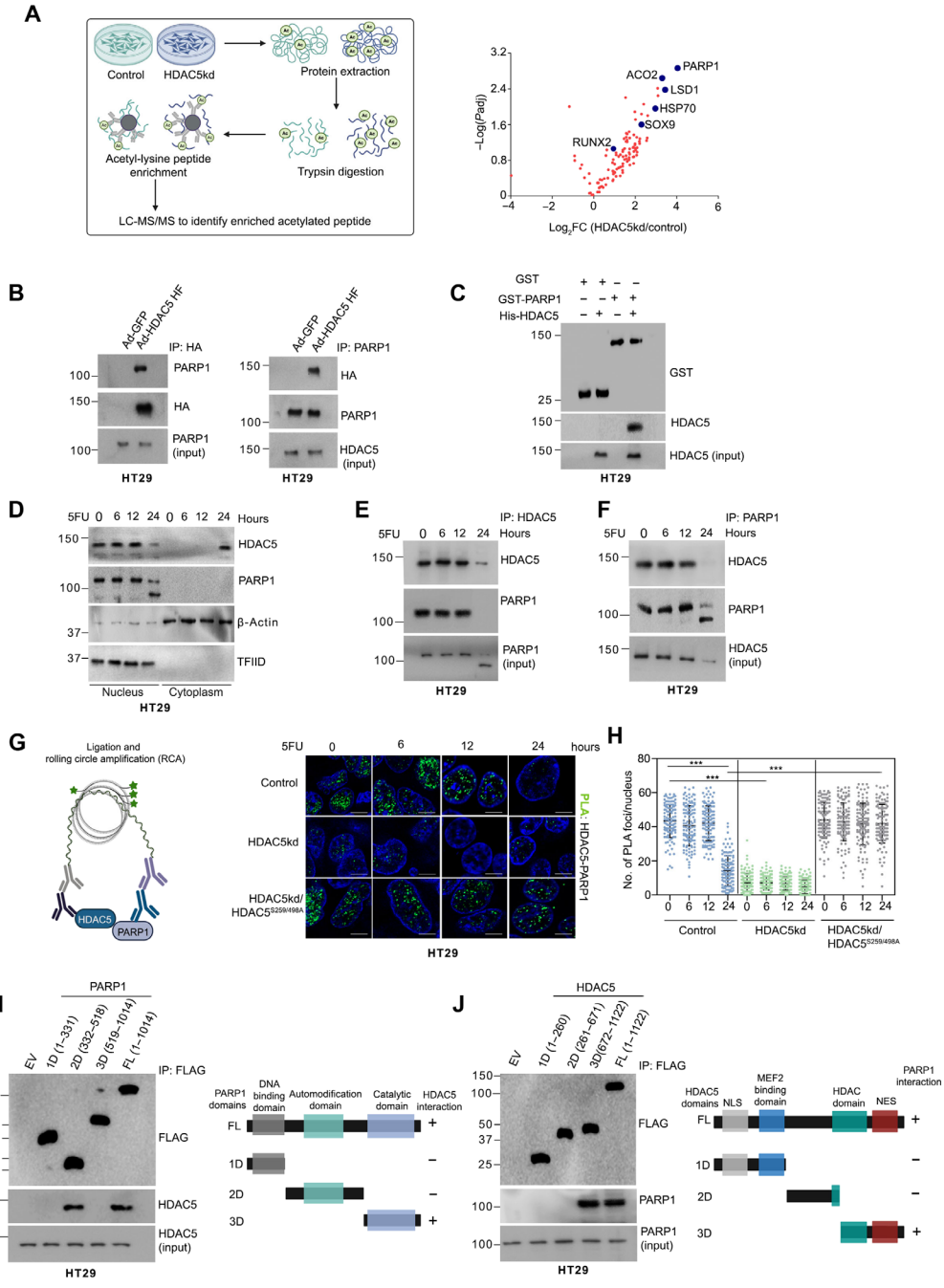

Fig. 1. PARP1 is an HDAC5-interacting protein. (**A**) Schematic workflow (left): HT29 cells were stably transfected with control (scrambled) or HDAC5 shRNA. Volcano plot of up-regulated acetylated peptides upon HDAC5 depletion (right). (**B**) HT29 cells were infected with indicated adenoviruses. Twenty-four hours after infection, immunoprecipitation (IP) followed by Western blotting was performed. HA, hemagglutinin. (**C**) Glutathione *S*-transferase (GST) pull-down assay was performed. Western blotting was then performed for the indicated proteins. (**D**) HT29 cells were treated with 5-fluorouracil (5FU; 10 μM) for indicated time points. Western blotting was then performed from nuclear and cytoplasmic extracts. (**E**) HT29 cells were treated with 5FU (10 μM) for indicated time points, and the nuclear extracts were subjected to immunoprecipitation followed by immunoblotting. (**F**) HT29 cells were treated with 5FU (10 μM) for indicated time points, and the nuclear extracts were subjected to immunoprecipitation. Western blotting was then performed. (**G** and **H**) HT29 control [Control; scrambled HDAC5 short hairpin RNA (shRNA)], HDAC5 knockdown (HDAC5kd; HDAC5 shRNA), and HDAC5 knockdown cells expressing HDAC5 mutant (HDAC5kd/HDAC5$^{S259/498A}$) were subjected to proximity ligation assay (PLA) [(G), left]. Representative images are shown [(G), right]. Scale bars, 10 μm. The number of PLA foci per cell was quantified and plotted (H). Statistical analyses were done using two-way analysis of variance (ANOVA) (Bonferroni's post hoc test). The data are representative of three independent experiments. Error bars are means ± SD. ***$P < 0.001$. (**I**) HT29 cells were transfected with an empty vector (EV) or the indicated FLAG-tagged PARP1 constructs. Twenty-four hours after transfection, nuclear extracts were subjected to immunoprecipitation. Western blotting was then performed (left). Schematic representation of the PARP1 full-length and deletion mutants (right). (**J**) HT29 cells were transfected as indicated. Twenty-four hours after transfection, nuclear extracts were subjected to immunoprecipitation. Western blotting was then performed (left). Schematic representation of the HDAC5 full-length and deletion mutants (right). (A), (G), (I), and (J) created with BioRender.com.

stress conditions including 5-fluorouracil (5FU) and cisplatin treatment. We observed that during the early phase of genotoxic stress (6 and 12 hours) when HDAC5 is nuclear, HDAC5 coimmunoprecipitated with PARP1 (Fig. 1, D and E, and fig. S1B). However, upon prolonged genotoxic stress (24 hours) when HDAC5 undergoes nuclear export (*14*), this interaction was lost. Reverse coimmunoprecipitation confirmed these findings (Fig. 1F and fig. S1C). Similar observations were also made in other cell types including SW480 and normal colon epithelial cells CCD 841 CoN (fig. S1, D to G). We further examined the interaction between PARP1 and HDAC5 by performing proximity ligation assay (PLA). The PLA foci were notably reduced upon prolonged genotoxic stress as compared to the early phase of genotoxic stress (Fig. 1, G and H). Moreover, upon HDAC5 depletion, the foci were diminished, while no decline was observed over the time course of genotoxic stress in the presence of a constitutively nuclear HDAC5 mutant (HDAC5$^{S259/498A}$).

To map the domain of PARP1 to which HDAC5 binds, we performed immunoprecipitation experiments using FLAG constructs expressing different domains of PARP1. The PARP1-FLAG segment containing 332 to 518 amino acids specifically bound to the HDAC5 protein (Fig. 1I). Using Flag-tagged constructs, we also mapped the domain of HDAC5, which binds to PARP1. We observed that the HDAC5-Flag segment containing amino acids 672 to 1122 bound to PARP1 (Fig. 1J). Together, these results indicate that the C-terminal deacetylase domain of HDAC5 binds to the automodification domain (BRCT) of PARP1.

HDAC5 deacetylates PARP1 at Lys^{498} and Lys^{521}

PARP1 has been reported to be acetylated by p300 which determines its transactivation function (*15*). To explore the functional consequence of PARP1-HDAC5 interaction, we examined PARP1 acetylation status upon genotoxic stress. Our results suggest that HDAC5 deacetylates PARP1 during the early phase of genotoxic stress (Fig. 2A). However, upon prolonged genotoxic stress when HDAC5 undergoes nuclear export, PARP1 was acetylated. Furthermore, upon HDAC5 depletion, PARP1 was constitutively acetylated over the time course of genotoxic stress. The PARP1 acetylation observed was p300-mediated as it was abolished upon p300 depletion (Fig. 2B).

To identify the site of PARP1 deacetylation, we mutated all five lysine residues of the BRCT domain reported to be acetylated by p300. We observed that the mutation of K498 and K521 residues results in the down-regulation of acetylation in the absence of HDAC5 (Fig. 2C). We performed an in vitro deacetylation assay using PARP1 peptides containing different acetylated lysine residues. MS analysis revealed that HDAC5 exhibits specific deacetylase activity toward the PARP1 peptides containing acetylated K498 and K521 residues (Fig. 2, D and E), which lie in the automodification domain of PARP1 and are well conserved (Fig. 2, F and G). We next examined the effect of HDAC5 on the PARP1 K498 and K521 acetylation status under genotoxic stress conditions. Acetylation at PARP1 K498 and K521 sites was observed only at extended periods of genotoxic stress concomitant to the decline in nuclear HDAC5 levels (Fig. 2H). On the other hand, in the absence of HDAC5, PARP1 K498 and K521 residues were constitutively acetylated over the time course of genotoxic stress. Similar results were obtained in other cell types (fig. S2, A to C). In addition, in the presence of deacetylase-dead HDAC5 mutant (HDAC5^{H893F}) PARP1 K498 and K521 acetylation remained unaltered upon genotoxic stress, which was abrogated in the presence of a constitutively nuclear HDAC5 mutant (HDAC5$^{S259/498A}$) (Fig. 2I). Previous studies suggest that homologous recombination repair (HRR) proteins determine PARP1's functions (*1*). Since the cell lines used in our study do not harbor a mutation in HRR genes (*16*, *17*), we further examined the effect of HRR factors BRCA1 and BRCA2 on HDAC5-mediated regulation of PARP1 acetylation status. Our results suggest that HDAC5 deacetylates PARP1 independent of the presence or absence of BRCA1 and BRCA2 (fig. S2, D and E). Together, these results suggest that HDAC5 deacetylates PARP1 at the conserved lysine 498 and lysine 521 residues. However, upon prolonged genotoxic stress when HDAC5 undergoes nuclear export, PARP1 is acetylated at these sites.

HDAC5-mediated deacetylation at Lys^{498} determines PARP1 DNA damage response

We next investigated the effect of PARP1 deacetylation on DNA damage response. We observed that upon prolonged genotoxic stress (24 hours), levels of phosphorylated histone H2AX (γH2AX), a DNA damage marker, were elevated concomitant to increased acetylated PARP1 levels due to a decline in nuclear HDAC5 levels. Likewise, γH2AX levels were also up-regulated upon HDAC5 depletion (Fig. 3A). However, in the presence of a constitutively nuclear HDAC5 mutant (HDAC5$^{S259/498A}$), γH2AX levels declined upon prolonged genotoxic stress together with down-regulation of acetylated PARP1 levels, but not in the presence of deacetylase-dead HDAC5 mutant (HDAC5^{H893F}). These results suggest that acetylation status determines PARP1-mediated DNA damage response.

Previous studies suggest that genotoxic stress results in DNA damage-induced PARP1 auto-PARylation which is determined by its acetylation status (*18*). We observed that upon prolonged stress, abrogation of HDAC5-mediated deacetylation inhibits PARP1 PARylation. Upon HDAC5 depletion or in the presence of deacetylase-dead HDAC5 mutant (HDAC5^{H893F}), PARylation was repressed throughout the course of genotoxic stress. On the other hand, in the presence of a constitutively nuclear HDAC5 mutant (HDAC5$^{S259/498A}$), PARP1 PARylation was observed throughout the course of genotoxic stress (Fig. 3B). We further examined the role of each of the sites of deacetylation in determining PARP1 PARylation upon genotoxic stress. We observed that PARylation was down-regulated in the case of acetyl-lysine mimic PARP1 mutant (PARP1^{K498Q}), but not in the case of acetyl-lysine mimic PARP1 mutant (PARP1^{K521Q}) and non-acetylable PARP1 mutants (PARP1^{K498R} and PARP1^{K521R}) (Fig. 3C). Upon HDAC5 depletion, PARylation was diminished in the case of PARP1^{K498Q}, PARP1^{K521Q}, and PARP1^{K521R} mutants but not in the case of PARP1^{K498R} mutant. These results suggest that Lys^{498} deacetylation plays a key role in determining PARP1 PARylation. PARylation has been reported to prevent cytotoxic PARP1 trapping onto the chromatin and facilitate DNA repair (*19*). Our data suggest that upon HDAC5 depletion or in the presence of deacetylase-dead HDAC5 mutant (HDAC5^{H893F}), there was increased PARP1 trapping but not in the presence of a constitutively nuclear HDAC5 mutant (HDAC5$^{S259/498A}$) (Fig. 3D). Furthermore, increased chromatin binding was observed in the case of acetyl-lysine mimic PARP1 mutant (PARP1^{K498Q}) but not in the case of a non-acetylable PARP1 mutant (PARP1^{K498R}). Thus, we concluded that K498 acetylation status plays a key role in determining PARP1 chromatin trapping.

We next examined the effect of acetylation status on PARP1-mediated recruitment of repair factors including MRE11 at sites of DNA damage (*3*). MRE11 participates in both HR and NHEJ repair

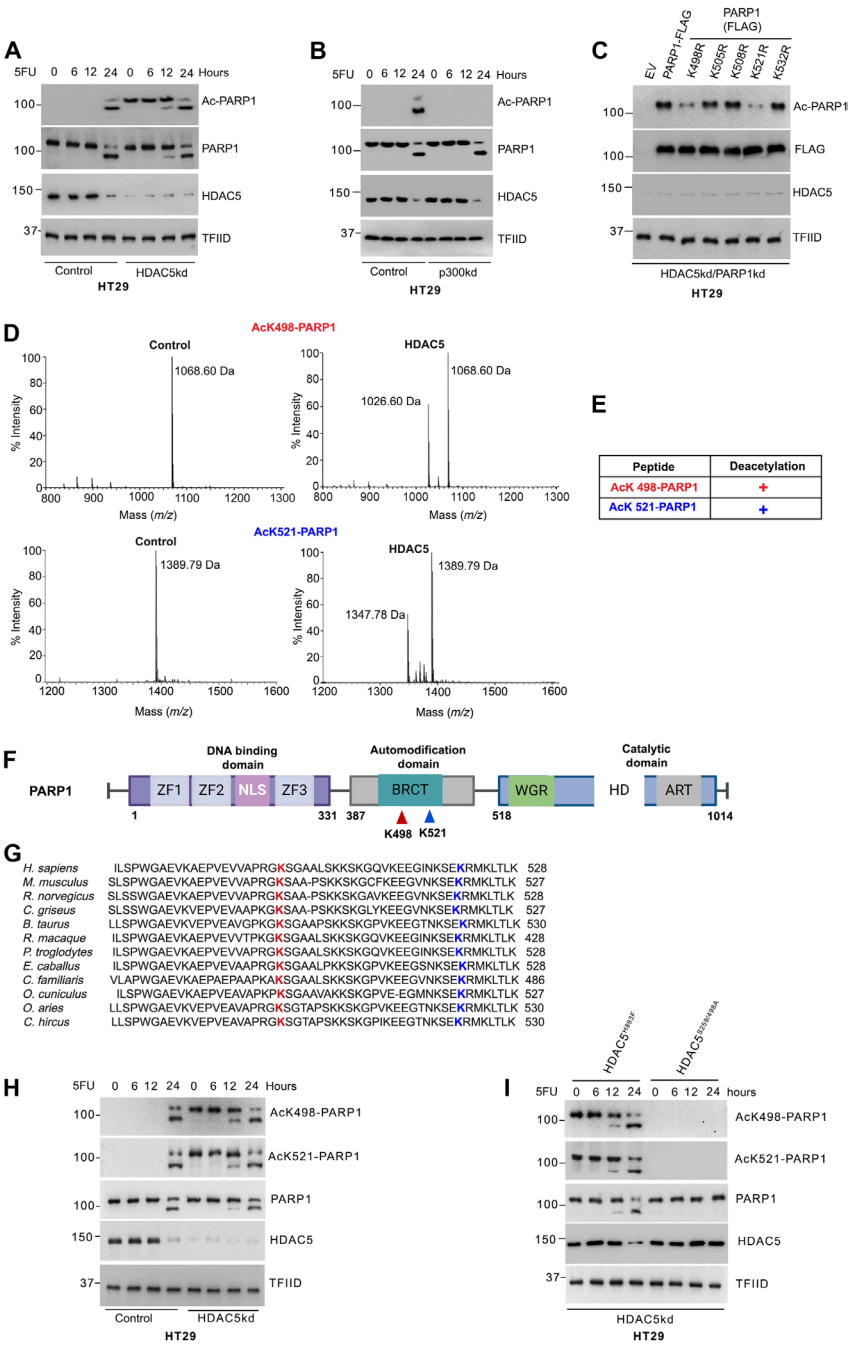

Fig. 2. PARP1 is deacetylated at Lys^{498} and Lys^{521} sites by HDAC5. (**A**) HT29 control (Control; scrambled HDAC5 shRNA) and HDAC5 knockdown (HDAC5kd; HDAC5 shRNA) cells were treated with 5FU (10 μM) for indicated time points. Western blotting was then performed for the indicated proteins from nuclear extracts. (**B**) HT29 cells were stably transfected (pooled zeomycin-resistant population) with control (Control; Scrambled p300 shRNA) or p300 knockdown (p300kd; p300 shRNA). These cells were treated with 5FU (10 μM) for indicated time points. Western blotting was then performed for the indicated proteins from nuclear extracts. (**C**) HT29 PARP1 and HDAC5 double knockdown (HDAC5kd/PARP1kd; HDAC5 and PARP1 shRNA) cells were transfected with FLAG-tagged wild-type PARP1, PARP1^{K498R}, PARP1^{K505R}, PARP1^{K508R}, PARP1^{K521R}, or PARP1^{K532R} constructs as indicated. Twenty-four hours after transfections nuclear extracts were prepared and subjected to immunoprecipitation followed by Western blotting for the indicated proteins. (**D**) AcK498-PARP1 and AcK521-PARP1 peptides were incubated either alone (Control) or in the presence of recombinant HDAC5. Mass spectrometry was then performed. The relative positions of acetylated Lys^{498} (1068.60 Da) and Lys^{521} (1389.79 Da), while deacetylated Lys^{498} (1026.60 Da) and Lys^{521} (1347.79 Da) PARP1 peptides are indicated. *m/z*, mass/charge ratio. (**E**) Results of HDAC5 deacetylation reactions using acetylated PARP1 peptides. (**F**) Schematic representation of the PARP1 domains. The lysine residues in the automodification domain are sites of HDAC5-mediated deacetylation. Created with BioRender.com. (**G**) The amino acid sequence encompassing human PARP1 K498 (red) and K521 (blue) residue. (**H**) HT29 control (Control; scrambled HDAC5 shRNA) and HDAC5 knockdown (HDAC5kd; HDAC5 shRNA) cells were treated with 5FU (10 μM) for indicated time points. Western blotting was then performed for the indicated proteins. (**I**) HT29 HDAC5 knockdown (HDAC5kd; HDAC5 shRNA) cells were stably transfected with Flag-tagged HDAC5 mutant constructs. These cells were treated with 5FU (10 μM) for indicated time points. Western blotting was then performed for the indicated proteins.

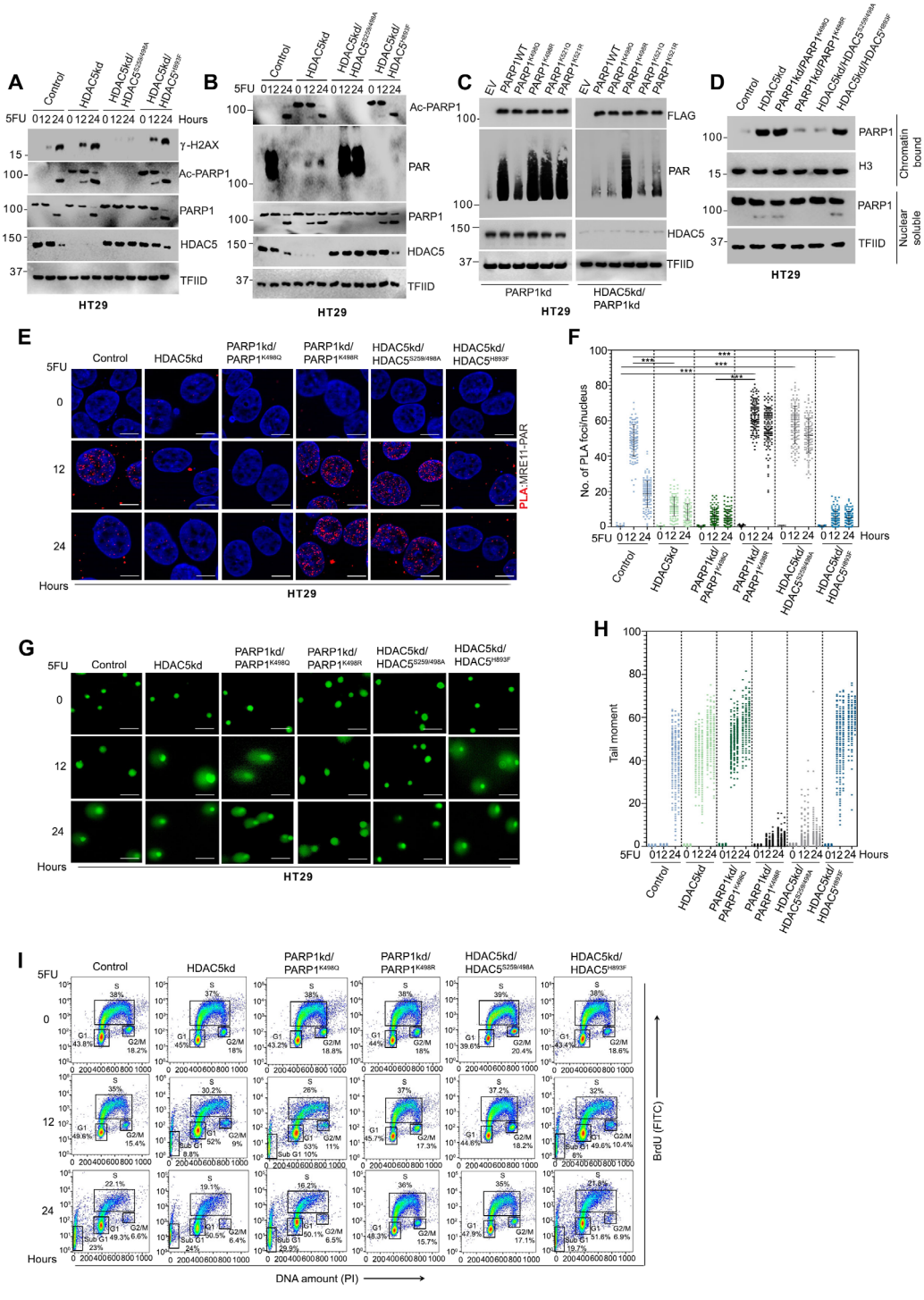

Fig. 3. Deacetylation of PARP1 at Lys^{498} by HDAC5 regulates DNA damage response. (**A**) Indicated cells were treated with 5FU (10 μM). Nuclear extracts were subjected to Western blotting was then performed for the indicated proteins. (**B**) Indicated cells were treated with 5FU (10 μM) for indicated time points. Nuclear extracts were prepared. Western blotting was then performed for the indicated proteins. (**C**) Indicated cells were treated with 5FU (10 μM) for 6 hours. Nuclear extracts were then prepared and subjected to Western blotting for the indicated proteins. (**D**) Indicated cells were treated with 5FU (10 μM) for 6 hours. The cells were harvested and Western blotting was performed for the indicated proteins from the nuclear and chromatin fractions. (**E** and **F**) Indicated cells were treated with 5FU (10 μM) for indicated time points. The cells were subjected to PLA. Representative images are shown (E). Scale bars, 10 μm. The number of PLA foci per cell was quantified and plotted as a nested scatter dot plot (F). Statistical analyses were done using two-way ANOVA (Bonferroni's post hoc test). The data are representative of three independent experiments. Error bars are means ± SD. ***$P < 0.001$. (**G** and **H**) Indicated cells were treated with 5FU (10 μM). The cells were cells subjected to alkaline comet assay (G). Scale bars, 50 μm. The tail moment of cells is shown in the nested scatter dot plot (H). The data are representative of three independent experiments. (**I**) Indicated cells were treated with 5FU (10 μM). 5-Bromo-2-deoxyuridine (BrdU) incorporation followed by fluorescence-activated cell sorting analysis was performed. FITC, fluorescein isothiocyanate.

pathways (*20*). It plays a critical role in the cellular decision of which mechanism will be used to repair damaged DNA. We observed a substantial decline in MRE11-PAR foci upon HDAC5 depletion or in the presence of HDAC5 mutant (HDAC5^{H893F}) from early periods of genotoxic stress (Fig. 3, E and F, and fig. S3, A to F). However, robust MRE11 recruitment was observed in the presence of HDAC5 mutant (HDAC5$^{S259/498A}$) or PARP1 mutant (PARP1^{K498R}). On the other hand, a notable reduction in foci was observed in the presence of PARP1 mutant (PARP1^{K498Q}). Thus, our data demonstrate that HDAC5-mediated deacetylation at Lys^{498} promotes PARP1 PARylation which facilitates recruitment of repair factors. We further assessed the effect of PARP1 acetylation status on DNA repair. We observed increased levels of DNA strand breaks upon HDAC5 depletion or in the presence of HDAC5 mutant (HDAC5^{H893F}) from early periods of genotoxic stress (Fig. 3, G and H, and fig. S3, G to I). Similar observations were made in the case of PARP1 mutant (PARP1^{K498Q}). However, the extent of DNA damage was notably reduced in the presence of HDAC5 mutant (HDAC5$^{S259/498A}$) or PARP1 mutant (PARP1^{K498R}). We also investigated the physiological implications of unresolved DNA damage. Our data suggest that HDAC5 depletion or the presence of HDAC5 mutant (HDAC5^{H893F}) results in increasing G1 arrest and cell death (sub-G1 population) from the early period of genotoxic stress. Similar observations were made in the case of PARP1 mutant (PARP1^{K498Q}). However, no discernible G1 arrest or cell death was observed in the presence of HDAC5 mutant (HDAC5$^{S259/498A}$) and PARP1 mutant (PARP1^{K498R}) over the time course of genotoxic stress (Fig. 3I and fig. S3, J to L). These results suggest that HDAC5-mediated deacetylation at the K498 site plays a pivotal role in determining PARP1-dependent DNA damage response.

Lys^{521} deacetylation enables PARP1 to function as ATF4 coactivator

To unravel the functional relevance of K521 acetylation status, we used a biochemical approach (Fig. 4A, left). We observed that many proteins specifically interacted with a non-acetylable PARP1 mutant (PARP1^{K521R}) but not with acetyl-lysine mimic PARP1 mutant (PARP1^{K521Q}) upon genotoxic stress (Fig. 4A, right). Among the most prominent interacting proteins, interaction with activating transcription factor 4 (ATF4) was notably reduced with acetyl-lysine mimic PARP1 mutant (PARP1^{K521Q}) but not so with wild-type PARP1 or acetyl-lysine mimic PARP1 mutant (PARP1^{K498Q}) (Fig. 4B). The interaction was also observed with a non-acetylable PARP1 mutant (PARP1^{K498R}). These data indicate that Lys^{521} acetylation status determines PARP1 interaction with ATF4. We further examined the kinetics of PARP1-ATF4 interaction under genotoxic stress conditions. We observed that during the early phase of genotoxic stress (12 hours), PARP1 coimmunoprecipitated with ATF4. However, upon prolonged stress, the interaction was lost. Reverse coimmunoprecipitation also corroborated these observations (fig. S4A). Similar results were obtained upon depletion of BRCA1 or BRCA2 (fig. S4, B and C). We further examined the interaction between PARP1 and ATF4 by performing PLA. Our results indicate that PLA foci were up-regulated at the early phase of genotoxic stress but declined upon prolonged stress concomitant to PARP1 acetylation (Fig. 4, C and D). Substantially reduced foci were observed upon HDAC5 depletion or in the presence of deacetylase-dead HDAC5 mutant (HDAC5^{H893F}). The foci were also similarly diminished in the presence of acetyl-mimetic PARP1 mutant (PARP1^{K521Q}). However, increased PLA foci were observed in the presence of a non-acetylable PARP1 mutant (PARP1^{K521R}) and a constitutively nuclear HDAC5 mutant (HDAC5$^{S259/498A}$). Thus, our results suggest that HDAC5 determines PARP1-ATF4 interaction under genotoxic stress conditions. We further examined whether HDAC5 regulates ATF4 levels. As has been previously reported, we also observed that ATF4 levels are induced by genotoxic stress (Fig. 4E) (*21*). However, HDAC5 depletion did not affect ATF4 levels.

Since ATF4 plays a pivotal role in stress response by regulating the expression of diverse genes (*22*), we next examined the impact of PARP1-ATF4 interaction on the cellular transcription program. We observed that under genotoxic stress conditions, PARP1 K521 acetylation status determines the expression of 2107 genes (Fig. 4F). Furthermore, ATF4 co-depletion results in down-regulation of 755 genes. Pathway enrichment analysis suggests that these genes are involved in cancer risk pathways including epithelial-to-mesenchymal transition (EMT)/metastasis and cell cycle regulation as well as metabolic pathways such as glutamine metabolism and amino acid biosynthesis (Fig. 5A). To gain further insights, we examined the effect of HDAC5-mediated PARP1 deacetylation on the expression of key ATF4-regulated genes involved in metabolism (*SLC1A5*, *GLS1*, and *GLUD1*), proliferation (*CCNB1*), and EMT (*MMP9*). Our results suggest that during the early phase of genotoxic stress, the transcript levels of these genes were up-regulated, but upon prolonged stress, the levels declined concomitantly to the loss of PARP1-ATF4 interaction. Furthermore, HDAC5 depletion or the presence of deacetylase-dead HDAC5 mutant (HDAC5^{H893F}) resulted in the down-regulation of these genes under genotoxic stress conditions (Fig. 4G and fig. S5, B to D). On the other hand, in the presence of a constitutively nuclear HDAC5 mutant (HDAC5$^{S259/498A}$), a notable increase in transcript levels of these genes was observed over the course of genotoxic stress. Thus, the presence of a non-acetylable PARP1 mutant (PARP1^{K521R}) robustly induces the transcript levels of these genes, while in the presence of acetyl-lysine mimic PARP1 mutant (PARP1^{K521Q}), expression of these genes was down-regulated. These results suggest that HDAC5 plays a key role in determining PARP1-dependent ATF4-mediated transactivation. To corroborate our findings, we further examined the role of PAPR1 acetylation status in determining ATF4 recruitment at the promoter of these genes. We observed that upon genotoxic stress, increasing levels of ATF4 were recruited at the promoters of these genes. Furthermore, the absence of HDAC5 or PARP1 acetylation status did not affect ATF4 recruitment (figs. S6A, left; and S7, A to C, left). To ascertain the presence of PARP1 in the transcription complex, we performed reChIP assay (fig. S6A, right; and S7, A to C, right). Our results suggest that increasing levels of PARP1 were detected at the promoters at the early phase of genotoxic stress which declined upon prolonged stress. In the absence of HDAC5 or in the presence of deacetylase-dead HDAC5 mutant (HDAC5^{H893F}), PARP1 presence at the promoters was down-regulated under genotoxic stress conditions. On the other hand, in the presence of a constitutively nuclear HDAC5 mutant (HDAC5$^{S259/498A}$), notably higher levels of PARP1 were observed at these promoters. Thus, high levels of a non-acetylable PARP1 mutant (PARP1^{K521R}) were detected at these promoters throughout the course of genotoxic stress, while no notable levels of acetyl-lysine mimic PARP1 mutant (PARP1^{K521Q}) could be detected. Together, these results suggest that HDAC5 regulates PARP1-dependent ATF4 transactivation function.

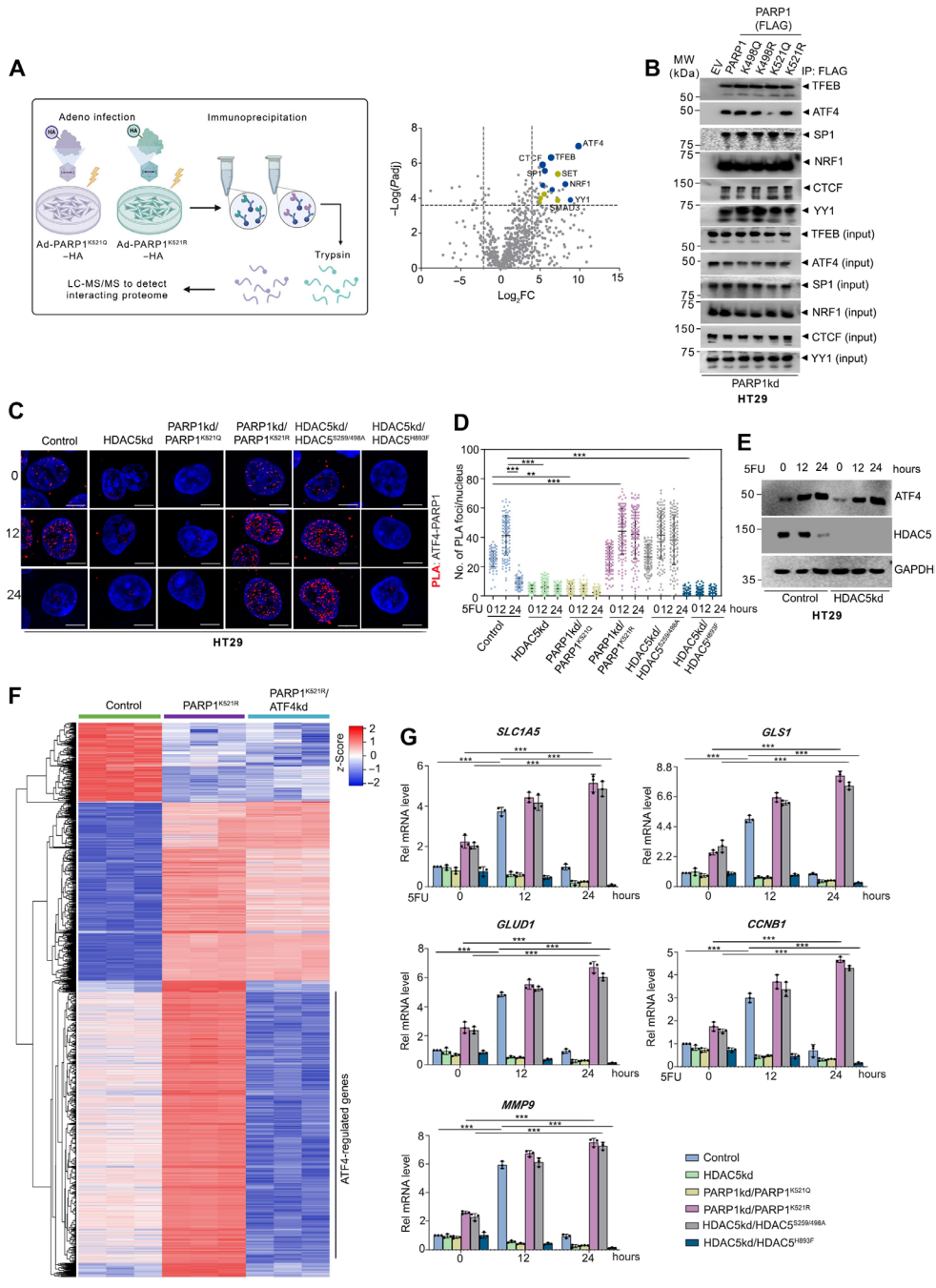

Fig. 4. HDAC5-mediated deacetylation at Lys^{521} modulates PARP1 coactivator function. (**A**) Schematic representation of workflow to identify mutant PARP1 binding proteins upon 5FU (10 μM) treatment for 12 hours in HT29 cells (left). Volcano plot of proteins interacting with PARP1 mutant (PARP1^{K521R}) (right). Created with BioRender.com. (**B**) HT29 PARP1 knockdown (PARP1kd; PARP1 shRNA) cells were transfected with EV or FLAG-tagged wild-type or mutant PARP1 constructs as indicated. Twenty-four hours after transfection, the cells were treated with 5FU (10 μM) for 12 hours. Immunoprecipitation followed by Western blotting for the indicated proteins was performed. (**C** and **D**) HT29 control (Control; Luc shRNA), HDAC5 knockdown (HDAC5kd; HDAC5 shRNA), and PARP1 knockdown cells (PARP1kd; PARP1 shRNA) expressing PARP1 mutants and HDAC5 knockdown cells expressing HDAC5 mutants were treated with 5FU (10 μM) for indicated time points. PLA was performed (C). Scale bars, 10 μm. The number of PLA foci per cell was quantified and plotted (D). Statistical analyses were done using two-way ANOVA (Bonferroni's post hoc test). Error bars are means ± SD. $^{**}P < 0.01$; $^{***}P < 0.001$. (**E**) HT29 control (Control) and HDAC5 knockdown (HDAC5kd) cells were treated with 5FU (10 μM) for indicated time points. Western blotting was then performed. GAPDH, glyceraldehyde-3-phosphate dehydrogenase. (**F**) HT29 control (Control; Luc shRNA), PARP1 knockdown cells expressing PARP1^{K521R} (PARP1^{K521R}), as well as PARP1 and activating transcription factor 4 (ATF4) double knockdown cells (PARP1 and ATF4 shRNA) expressing PARP1^{K521R} (PARP1^{K521R}/ATF4kd) were treated with 5FU and subjected to RNA sequencing analysis. Red and blue indicate up-regulation and down-regulation, respectively. (**G**) HT29 control (Control; Luc shRNA), HDAC5 knockdown (HDAC5kd), PARP1 knockdown cells expressing PARP1 mutants, and HDAC5 knockdown cells expressing HDAC5 mutants were treated with 5FU (10 μM) for indicated time points. A reverse transcription quantitative polymerase chain reaction was performed. Statistical analyses were done using two-way ANOVA (Tukey's post hoc test). Error bars are means ± SD of three independent experiments with triplicate samples. $^{***}P < 0.001$.

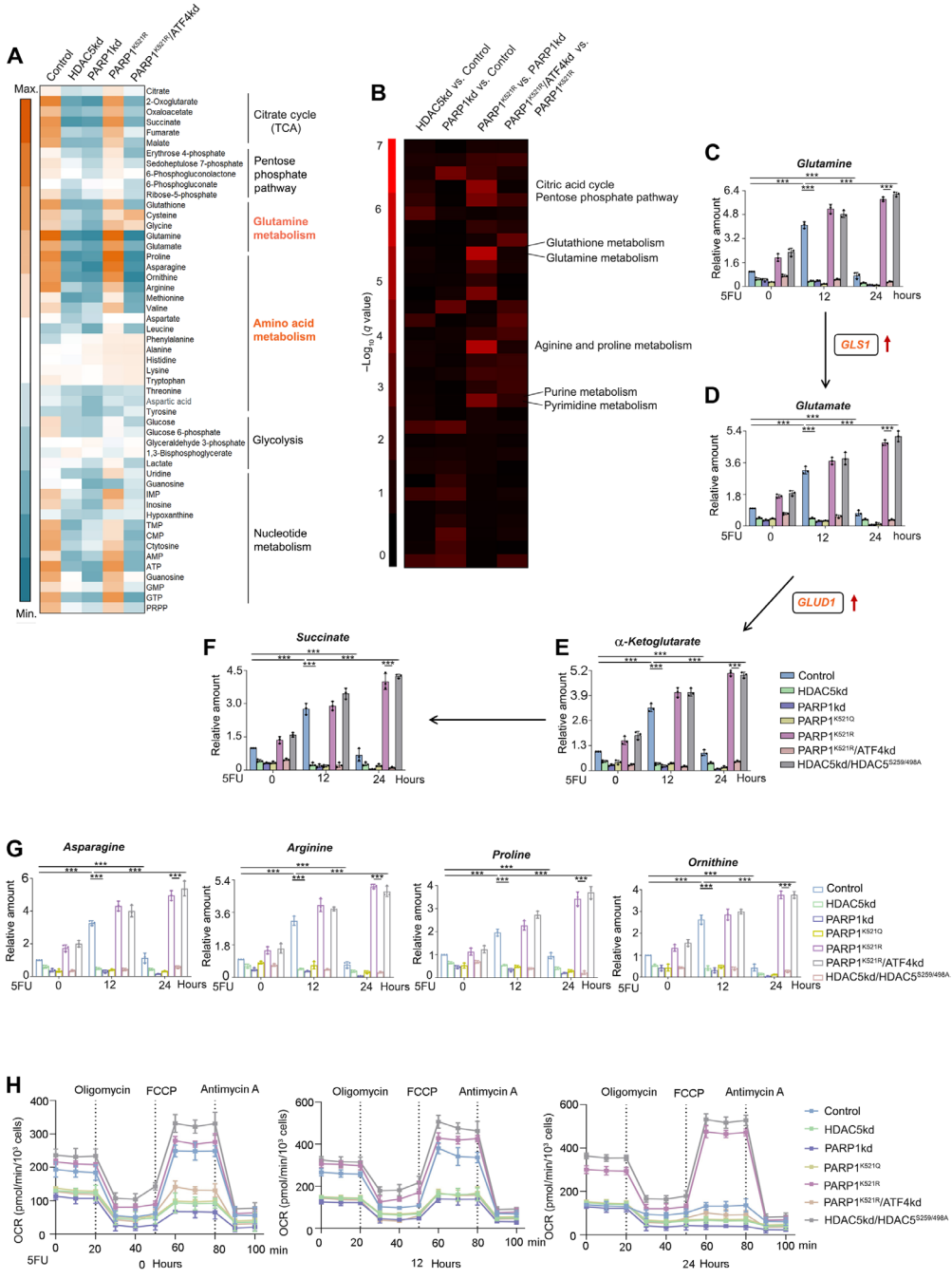

Fig. 5. PARP1 K521 acetylation status determines metabolic response upon genotoxic stress. (**A**) HT29 control (Control; Luc shRNA), HDAC5 knockdown (HDAC5kd; HDAC5 shRNA), PARP1 knockdown (PARP1kd; PARP1 shRNA), PARP1 knockdown cells expressing PARP1^{K521R} (PARP1^{K521R}), as well as PARP1 and ATF4 double knockdown cells expressing PARP1^{K521R} (PARP1^{K521R}/ATF4kd) were treated with 5FU (10 μM) for 12 hours. The metabolites were extracted from the harvested cells and analyzed by liquid chromatography–mass spectrometry (LC-MS). Relative levels of specific metabolites normalized to cell number are shown in the heatmap. The heatmap depicts relative changes in intracellular metabolites. Orange and cyan indicate up-regulation and down-regulation, respectively. (**B**) Metabolic pathway enrichment analysis of (A). Metabolite data are representative of three independent experiments. (**C** to **G**) HT29 control (Control), HDAC5 knockdown (HDAC5kd), PARP1 knockdown (PARP1kd), PARP1 knockdown cells expressing PARP1^{K521Q} (PARP1^{K521Q}) or PARP1^{K521R} (PARP1^{K521R}), PARP1 and ATF4 double knockdown cells expressing PARP1^{K521R} (PARP1^{K521R}/ATF4kd), as well as HDAC5 knockdown cells expressing HDAC5$^{S259/498A}$ (HDAC5kd/HDAC5$^{S259/498A}$) were treated with 5FU (10 μM) for indicated time points. The cells were harvested, and metabolites were extracted. The relative amounts of the indicated metabolites were quantified using respective kits. Statistical analyses were done using two-way ANOVA (Bonferroni's post hoc test). The data are representative of three independent experiments. Error bars are means ± SD. ***$P < 0.001$. (**H**) HT29 control (Control), HDAC5 knockdown (HDAC5kd), PARP1 knockdown (PARP1kd), as well as PARP1 knockdown cells expressing PARP1^{K521Q} (PARP1kd/PARP1^{K521Q}) or PARP1^{K521R} (PARP1kd/PARP1^{K521R}), PARP1 and ATF4 double knockdown cells expressing PARP1^{K521R} (PARP1^{K521R}/ATF4kd), and HDAC5 knockdown cells expressing HDAC5$^{S259/498A}$ (HDAC5kd/HDAC5$^{S259/498A}$) were treated with 5FU (10 μM) for indicated time points. The cellular oxygen consumption rate (OCR) was then measured. The data are representative of three independent experiments.

PARP1-ATF4 promotes metabolic adaptation

Since our transcriptomics data suggests that PARP1 K521 acetylation status determines the expression of several metabolic genes, we performed an unbiased analysis to comprehend its role in the metabolic response under genotoxic stress conditions. Among diverse pathways, we observed prominent enrichment in pathways associated with glutamine and amino acid metabolism (Fig. 5, A and B). Glutamine has been reported to serve as a carbon source for tricarboxylic acid (TCA) cycle intermediates to support the energy requirement of cancer cells (*23*). Upon HDAC5 or PARP1 depletion, the levels of several key intermediate metabolites involved in glutamine and amino acids metabolism declined under genotoxic stress conditions. However, increased levels of these metabolites were observed in the presence of a non-acetylable mutant ($PARP1^{K521R}$) but were down-regulated upon ATF4 co-depletion. We further examined the effect of PARP1 K521 acetylation status on glutamine utilization and amino acid biosynthesis over the course of genotoxic stress. Our results indicated that the levels of glutamine-derived intermediates (*Glutamine*, *Glutamate*, *a-Ketoglutarate*, and *Succinate*) along with amino acids (*Asparagine*, *Arginine*, *Proline*, and *Ornithine*) were induced at early time points of genotoxic stress but the levels declined upon prolonged stress (Fig. 5, C to G, and fig. S8, A to C). HDAC5 or PARP1 depletion resulted in down-regulation of these metabolites over the course of genotoxic stress. In the presence of a constitutively nuclear HDAC5 mutant ($HDAC5^{S259/498A}$), the levels of these metabolites were elevated, while reduced levels were detected in the presence of acetyl-lysine mimic PARP1 mutant ($PARP1^{K521Q}$) over the time course of genotoxic stress. On the other hand, in the presence of a non-acetylable PARP1 mutant ($PARP1^{K521R}$), increasing levels of these metabolites were observed which were down-regulated upon ATF4 co-depletion. To corroborate our findings, we also examined the effect of PARP1 K521 acetylation status on cellular energetics. OCR (oxygen consumption rate) levels were elevated at the early phase of genotoxic stress but declined upon prolonged stress (Fig. 5H). A notable decline in OCR levels was also observed upon HDAC5 or PARP1 depletion under genotoxic stress conditions. Elevated OCR levels were observed in the presence of a constitutively nuclear HDAC5 mutant ($HDAC5^{S259/498A}$), while reduced levels were observed in the presence of acetyl-lysine mimic PARP1 mutant ($PARP1^{K521Q}$) over the time course of genotoxic stress. In addition, in the presence of a non-acetylable PARP1 mutant ($PARP1^{K521R}$), increasing OCR levels were observed which declined upon ATF4 co-depletion. These results suggest that during the early phase of genotoxic stress, PARP1-ATF4 interaction promotes metabolic adaptation, which is perturbed upon prolonged stress due to PARP1 acetylation at the K521 site and subsequent loss of interaction with ATF4.

HDAC5 augments PARP1 oncogenic potential

We next investigated the effect of PARP1 acetylation status on malignant phenotype under genotoxic stress conditions. We observed that the depletion of HDAC5 or PARP1 resulted in reduced proliferation capacity, while the presence of a constitutively nuclear HDAC5 mutant ($HDAC5^{S259/498A}$) increased proliferation capacity (Fig. 6, A and B, and fig. S9, A to D). Proliferation capacity was also higher in the presence of non-acetylable PARP1 mutants, $PARP1^{K498R}$, $PARP1^{K521R}$, and $PARP1^{K498R/K521R}$, which was down-regulated upon treatment with pharmacological PARP1 inhibitor olaparib in the case of $PARP1^{K498R}$ but not in the case of $PARP1^{K498R/K521R}$. More robust down-regulation was observed in the case of stronger PARP1 inhibitor talazoparib (fig. S9, E and F) (*19*). We next examined the effect of HDAC5-mediated PARP1 deacetylation on invasiveness and migration potential. Our results suggest that invasiveness and migration potential declined upon depletion of HDAC5 or PARP1 under genotoxic stress conditions but was up-regulated in the presence of a constitutively nuclear HDAC5 mutant ($HDAC5^{S259/498A}$) (Fig. 6, C and D, and fig. S10, A to D). In addition, in the presence of non-acetylable PARP1 mutants, $PARP1^{K498R}$, $PARP1^{K521R}$, and $PARP1^{K498R/K521R}$, invasiveness and migration potential were elevated, which was repressed upon olaparib treatment in the case of $PARP1^{K498R}$ but not in the case of $PARP1^{K498R/K521R}$. The repression was more prominent in the case of talazoparib treatment (fig. S10, E and F).

Since our data suggest that PARP1 induces the expression of genes associated with EMT in an ATF-dependent manner, we further investigated the effect on cellular morphology and EMT markers. We observed that under genotoxic stress conditions, the presence of a non-acetylable PARP1 mutant ($PARP1^{K521R}$) or a constitutively nuclear HDAC5 mutant ($HDAC5^{S259/498A}$) induced cellular morphological changes indicative of EMT with loss of cell-cell contacts and cell scattering (fig. S10G). The cellular morphological changes were corroborated by the reduced levels of epithelial marker E-cadherin and up-regulation of mesenchymal markers vimentin and fibronectin (fig. S10H). On the other hand, the presence of acetyl-lysine mimics PARP1 mutant ($PARP1^{K521Q}$), and depletion of HDAC5 or PARP1 did not induce EMT.

We further investigated the effect of HDAC5-PARP1 interplay on tumorigenicity. Tumor growth was attenuated upon HDAC5 or PARP1 depletion, while substantially larger tumors were observed in the presence of HDAC5 mutant ($HDAC5^{S259/498A}$) (Fig. 6, E and F). Moreover, non-acetylable PARP1 mutants, $PARP1^{K498R}$, $PARP1^{K521R}$, and $PARP1^{K498R/K521R}$, promoted tumor growth, which was suppressed upon olaparib treatment in the case of $PARP1^{K498R}$ but not in the case of $PARP1^{K498R/K521R}$. The inhibition of tumor growth was more prominent in the case of talazoparib treatment (fig. S11, A to C). The increased tumor size promoted by the HDAC5-PARP1 axis was corroborated by higher Ki67 and CD31 staining, which are indicative of higher proliferation rate and angiogenesis, respectively, along with a concurrent reduction in γH2AX and terminal deoxynucleotidyl transferase–mediated

deoxyuridine triphosphate nick end labeling (TUNEL) staining indicative of reduced DNA damage and apoptosis, respectively (Fig. 6, G to K). Together, our results suggest that HDAC5-mediated deacetylation plays a critical role in determining PARP1 oncogenic potential. Both the DNA repair and transactivation functions of PARP1 determined by the acetylation status of K498 and K521 sites, respectively, play a critical role in PARP1-mediated tumorigenesis. Thus, olaparib, a PARP1 DNA damage response inhibitor, does not sufficiently inhibit tumorigenesis as PARP1 transactivation function remains unperturbed.

HDAC5 is critical for PARP1-induced aggressive tumor phenotype

We next investigate the role of HDAC5 in PARP1-induced tumor malignancy in orthotopic colon cancer model. Our data suggest that abrogation of HDAC5 or PARP1 expression results in reduced tumor growth, while the presence of a constitutively nuclear HDAC5 mutant ($HDAC5^{S259/498A}$) promotes a notable increase in tumor size under genotoxic stress conditions (Fig. 7, A and B). Furthermore, numerous metastatic nodules were detected in the lung and

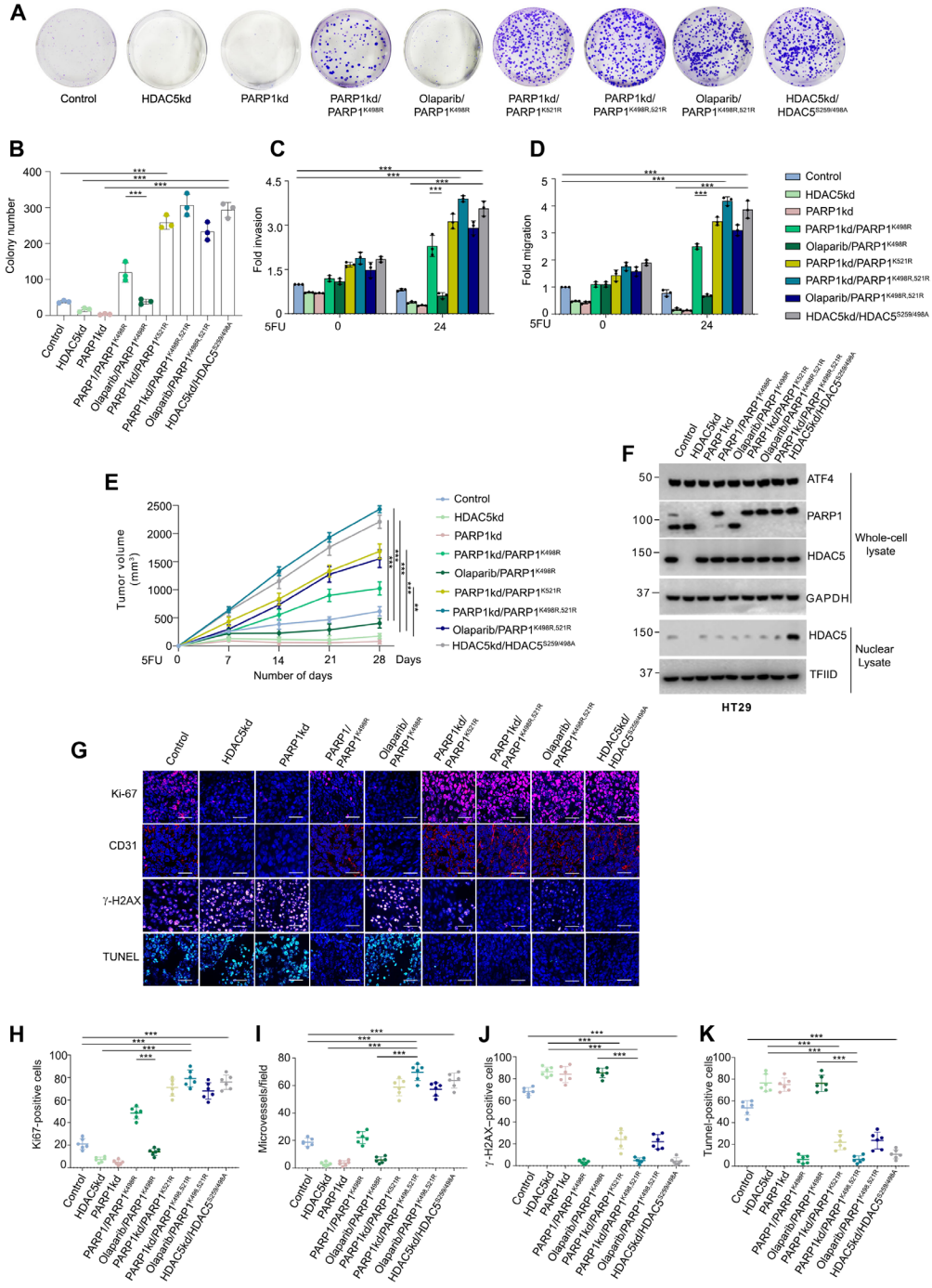

Fig. 6. HDAC5-mediated deacetylation induces PARP1 oncogenic functions. (**A** and **B**) Indicated cells were treated with 5FU (4 μM). Cells were also subjected to olaparib cotreatment (5 mM) as indicated. Colonies were enumerated after 7 days. Representative images are shown (A). Results were plotted as a number of colonies formed after 7 days (B). Statistical analyses were done using one-way ANOVA (Tukey's post hoc test). The data are representative of three independent experiments. Error bars are means ± SD. ***$P < 0.001$. (**C**) Indicated cells were treated with 5FU (10 μM). Cells were also subjected to olaparib cotreatment (5 mM) as indicated. In vitro invasion potential was measured. Error bars are means ± SD of three independent experiments with triplicate samples. ***$P < 0.001$. (**D**) Indicated cells were treated with 5FU (10 μM). Cells were also subjected to olaparib cotreatment (5 mM) as indicated. The migration potential was then measured. Error bars are means ± SD of three independent experiments with triplicate samples. ***$P < 0.001$. (**E**) Indicated cells were subcutaneously injected into the right flank of nude mice. After 1 week of injection, the mice were administered 5FU (25 mg/kg) every alternate day. Olaparib was also coadministered at a dose of 10 mg/kg daily as indicated. Tumor volume was measured on the indicated days. The data are representative of three independent experiments ($n = 5$ mice per group). Error bars represent means ± SD from five individual mice. **$P < 0.01$; ***$P < 0.001$. Statistical analyses were done using one-way ANOVA (Tukey's post hoc test). (**F**) Tumor lysates [(E) above] were subjected to Western blotting. (**G** to **K**) Immunohistochemical analysis was performed on the tumor sections from (E) above (G). Scale bars, 50 μm. The relative intensity was quantified and represented as means ± SD of three independent experiments [(G) to (K)]. ***$P < 0.001$. Statistical analyses were done using one-way ANOVA (Tukey's post hoc test).

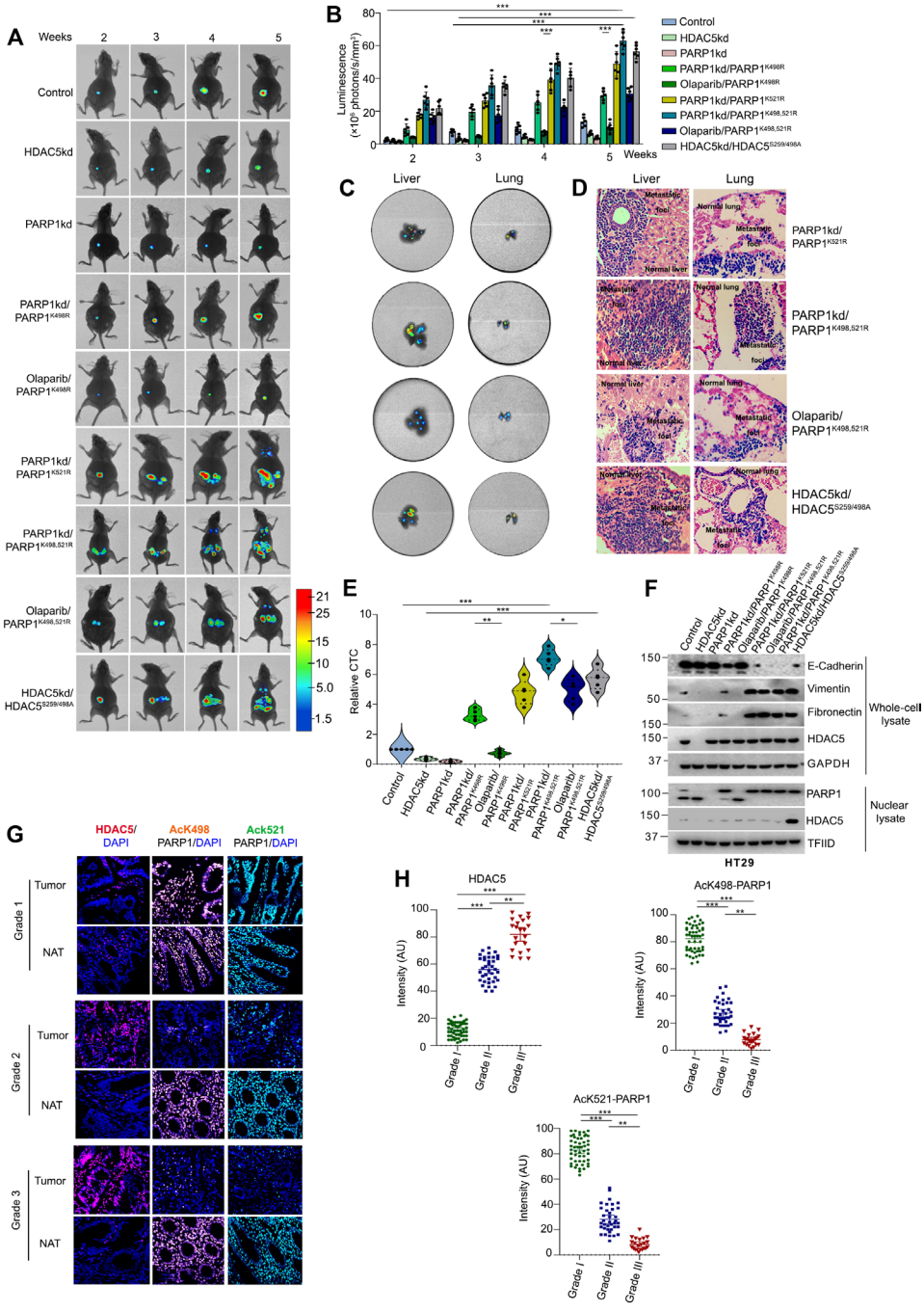

Fig. 7. PARP1 promotes aggressive tumor phenotype in an HDAC5-dependent manner. (**A**) HT29^{Luc2} control (Control; Luc shRNA); HDAC5 knockdown (HDAC5kd; HDAC5 shRNA); PARP1 knockdown (PARP1kd; PARP1 shRNA); PARP1 knockdown cells (PARP1kd; PARP1 shRNA) expressing PARP1^{K498R} (PARP1kd/PARP1^{K498R}), PARP1^{K521R} (PARP1kd/PARP1^{K521R}), or PARP1^{K498R,521R} (PARP1kd/PARP1^{K498R,521R}); and HDAC5 knockdown cells expressing HDAC5$^{S259/498A}$ (HDAC5kd/HDAC5$^{S259/498A}$) were orthotopically injected into the cecum wall of nude mice. After 1 week, mice were administered 5FU (10 mg/kg) every alternate day. Olaparib was also coadministered at a dose of 10 mg/kg daily as indicated. Bioluminescence imaging was performed. (**B**) Bioluminescence quantification [(A) above]. The data are representative of three independent experiments using five individual mice per group. Error bars are means ± SD from five individual mice ($n = 5$ mice per group). Statistical analyses were done using two-way ANOVA (Tukey's post hoc test). ***$P < 0.001$. (**C** and **D**) At the end of 5 weeks, the liver and lung from indicated mice [(A) above] were analyzed by ex vivo imaging (C) and hematoxylin and eosin staining (D). (**E**) At the end of 5 weeks, the blood from mice in (A) above was used to isolate genomic DNA for examining circulating tumor cells. The data are representative of three independent experiments using five individual mice per group. Error bars are means ± SD from five individual mice ($n = 5$ mice per group) *$P < 0.05$; **$P < 0.01$; ***$P < 0.001$. (**F**) At the end of 5 weeks, lysates of primary orthotopic tumors from (A) above were analyzed by immunoblotting for the indicated proteins. (**G** and **H**) Representative image of immunostaining of the indicated proteins in different grades of colon adenocarcinoma and matched normal adjacent tissue (NAT) (G). Quantitation of HDAC5, AcK498-PARP1, and AcK521-PARP1 levels (H). Statistical analyses were done using one-way ANOVA (Dunn's multiple comparison test). Error bars are means ± SD. **$P < 0.01$; ***$P < 0.001$.

liver (Fig. 7, C and D). Likewise, non-acetylable PARP1 mutants, PARP1^{K498R}, PARP1^{K521R}, and PARP1$^{K498R/K521R}$, induced robust tumor growth and metastasis, which was suppressed upon olaparib treatment in the case of PARP1^{K498R} but not in the case of PARP1$^{K498R/K521R}$. The mice with metastatic tumors also exhibited higher number of circulating tumor cells in these mice (Fig. 7E). This was further corroborated by the reduced levels of epithelial marker E-cadherin and up-regulation of mesenchymal markers vimentin and fibronectin in the primary tumors, which is indicative of predisposition of these tumors to metastasize (Fig. 7F). Thus, our data demonstrate that HDAC5 is a key determinant of PARP1-promoted tumor growth and metastasis. Since HRR proteins determine sensitivity to PARP inhibitors, we further examined the response to olaparib treatment in BRCA1/2-deficient orthotopic tumors (*24*). We observed that repression of tumor growth and metastasis upon olaparib treatment in the case of PARP1^{K498R} was more robust in BRCA1/2-deficient tumors (fig. S12, A to F).

Previous reports suggest that dysregulation of HDAC5 is associated with colon adenocarcinoma (*25*). Hence, we next examined HDAC5 levels and PARP1 acetylation status in different grades of colon adenocarcinoma. We observed that HDAC5 levels were elevated in colon adenocarcinoma as compared to matched normal adjacent tissue. Moreover, with increasing grades of colon adenocarcinoma, HDAC5 levels were up-regulated, while AcK498-PARP1 and AcK521-PARP1 levels declined (Fig. 7, G and H). Thus, our results suggest that dysregulation of HDAC5 and consequent perturbation in PARP1 acetylation status plays a critical role in determining colon cancer progression.

DISCUSSION

PARP1 is an abundant nuclear protein with well-documented roles in both DNA repair and transcription. Previous studies suggest that the transactivation and repair functions of PARP1 could be modulated by posttranslational modifications including mono-ADP-ribosylation and acetylation. Sirt6 mono-ADP-ribosylates PARP1 thereby inducing its enzymatic activity and augmenting DNA repair under genotoxic stress conditions (*26*). p300/CBP has been reported to acetylate PARP1 in response to inflammatory stimuli (*15*). Acetylated PARP1 serves as a coactivator for nuclear factor κB (NF-κB)–dependent transcription. Histone deacetylase inhibitors have also been reported to trigger PARP1 acetylation. Acetylation of PARP1 promotes chromatin trapping and reduces repair efficiency (*27*). Our studies provide a concerted mechanism for the dynamic regulation of both DNA repair and transactivation functions of PARP1. Using a biochemical approach, we have established HDAC5 as the bona fide deacetylase determining PARP1 acetylation status under genotoxic stress conditions. HDAC5-mediated PARP1 deacetylation at the K498 site augments repair function and prevents cell death. On the other hand, HDAC5-mediated deacetylation at the K521 site promotes PARP1 coactivator function in ATF4-mediated transactivation. Moreover, the functional consequences of deacetylation at these sites were mutually exclusive. In the absence of HDAC5 both, the sites were acetylated in a p300-dependent manner. Thus, our study establishes a preeminent role for acetylation status in determining PARP1's functions.

PARP1-dependant transcriptional regulation has been reported to play a key role in several human malignancies (*5*). PARP1 regulates gene expression by functioning as part of enhancer/promoter binding complexes. Furthermore, PARP1 has been reported to serve as a coactivator of transcription factors including NF-κB and hypoxia-inducible factor 1α (HIF1α). PARP1 binds to NF-κB and is pivotal for the induction of target genes involved in tumor development (*28*, *29*). Likewise, PARP1 forms a complex with HIF1α involving direct interaction (*30*). This complex triggers the expression of genes that promote angiogenesis and inhibit apoptosis to promote tumorigenesis. To delineate the role of acetylation status in determining its transactivation status, we examined the PARP1 binding proteins. Our data indicate that HDAC5-mediated deacetylation at Lys^{521} site promotes PARP1 interaction with ATF4. ATF4 is a stress-induced transcription factor that is commonly up-regulated in several cancers. It induces the expression of genes involved in adaptive responses to stress conditions (*22*). We provide further insights to establish a role for PARP1 in ATF4-mediated induction of genes involved in diverse pathways including proliferation, metastasis, and metabolism to promote survival under stress conditions and to sustain rapid tumor growth. Thus, our findings add to the repertoire of transcription factors involved in PARP1-mediated transcriptional regulation.

PARP1 activated in response to genotoxic insult catalyzes PARylation, which uses nicotinamide adenine dinucleotide (NAD^+) as substrate. NAD^+ serves as a cofactor for several enzymes involved in cellular energy metabolism. Thus, PARP1 promotes a metabolic shift to oxidative phosphorylation over glycolysis to maintain homeostasis and promote cell survival (*31*). Furthermore, transketolase, a key enzyme of the pentose phosphate pathway, is PARylated by PARP1 upon DNA damage (*32*). PARylation inhibits transketolase enzymatic activity, which boosts ribose-5-phosphate levels required for DNA biosynthesis, thereby augmenting the repair process. In addition, the PARP1 transactivation function also determines metabolic flux. PARP1 interacts with transcription factors, including peroxisome proliferator–activated receptor α, to induce the expression of genes involved in lipid metabolism (*33*). Thus, inhibition of PARP1 alleviates lipid accumulation in mouse models of fatty liver. However, the role of PARP1 in metabolic rewiring in tumor cells is not well explored. Our study unravels PARP1's function in determining glutamine metabolism. PARP1-ATF4 induces the expression of metabolic genes that promote the glutamine anaplerotic pathway (*34*) to maintain cellular energetics. Glutamine also serves as the nitrogen source for amino acid and nucleic acid biosynthesis. Thus, PARP1-mediated transactivation is critical for metabolic adaptation to support rapid proliferation (fig. S13A). In conclusion, our findings highlight the significance of acetylation status in determining PARP1 oncogenic potential. HDAC5-mediated deacetylation at Lys^{498} provides a survival advantage by preventing the accumulation of damaged DNA upon genotoxic insult, while deacetylation at Lys^{521} modulates a transcriptional program that augments rapid proliferation and metabolic reprogramming. Thus, our study delineates the role of the PARP1-HDAC5 axis in determining malignant phenotype.

MATERIALS AND METHODS

Cell lines and culture conditions

HT29 and SW480 cells were cultured in Dulbecco's modified Eagle's medium (DMEM) supplemented with 10% fetal bovine serum (FBS; Invitrogen), penicillin (100 U/ml), and streptomycin (100 μg/ml) at 37°C. Human normal colon epithelial cells CCD 841 CoN were

cultured in Eagle's minimum essential medium supplemented with 10% FBS. The cell lines were obtained from the American Type Culture Collection. Recombinant adenoviruses were amplified, and titration was performed as previously reported (*35*). Cells were cultured to ~50 to 70% confluency followed by infection with recombinant adenovirus at a multiplicity of infection of 10 to 20. Adenovirus expressing green fluorescent protein was used as a negative control. To induce genotoxic stress, cells were grown to ~50% confluency and then treated with 5FU (Sigma-Aldrich) or oxaliplatin (Sigma-Aldrich).

Plasmids and shRNA

The Flag-tagged HDAC5 double mutant (HDAC5$^{S259A/S498A}$) was a gift from R, Shaw (Addgene, plasmid #32218). The PARP1 construct was a gift from T. Muir (Addgene, plasmid #111575). HDAC5^{H893F}, PARP1^{K498Q}, PARP1^{K521Q}, PARP1^{K498R}, PARP1^{K521R}, and PARP1^{K498,521R} mutant constructs were generated by site-directed mutagenesis (GCC Biotech, India). For the in vitro GST pull-down assay, HDAC5 was cloned in the pET-28a(+) vector, and PARP1 was cloned in pGEX-4T-1 to generate His and GST fusion proteins. For domain mapping, FLAG-tagged HDAC5 and PARP1 full-length and different domains were cloned in pcDNA3.1 vector to generate FLAG fusion proteins. Transfection was performed using Lipofectamine 3000 (Invitrogen) for HT29 and SW480, and Lipofectamine 2000 (Invitrogen) for CCD 841 CoN cells according to the manufacturer's instructions. In transient transfection experiments, plasmid DNA was kept constant with an empty vector. Recombinant adenovirus expressing HDAC5-HA-FLAG, PARP1-HA, and PARP1^{K521R}-HA was generated, as described previously (*36*).

Constructs expressing short hairpin RNA (shRNA) were generated using the psiRNA-DUO plasmid (Invivogen) which allows independent expression of two shRNAs. The shRNAs targeting human *HDAC5*, *PARP1*, and *ATF4* were designed against the 3′ untranslated region of the transcript and hence cannot target the ectopically expressed gene. The sequences used have been provided in table S1.

Determination of acetylation status of proteins

Biochemical analysis of acetylation was performed, as described previously (*37*). Briefly, acetylated peptides were enriched using anti–acetyl-lysine antibody (Cell Signaling Technology). The immunoaffinity-purified acetylated peptides were analyzed by liquid chromatography–tandem mass spectrometry (LC-MS/MS; Thermo Fisher Scientific).

Western blot and immunoprecipitation

Cells were lysed in ice-cold lysis buffer containing 20 mM tris·HCl (pH 7.4), 5 mM EDTA, 10 mM $Na_4P_2O_7$, 100 mM NaF, 2 mM Na_3VO_4, 1% NP-40, 1 mM phenylmethylsulfonyl fluoride, and 1× protease inhibitor mixture (Roche). Subcellular fractions were prepared using a Subcellular Protein Fractionation Kit (Thermo Fisher Scientific) following the manufacturer's instructions. SDS–polyacrylamide gel electrophoresis (SDS-PAGE) was performed using equal amounts of proteins for each sample and transferred to a PVDF membrane (Millipore). All blots were imaged using a chemiluminescent Western blot imaging system (Azure Biosystems). The antibodies are listed in table S2. A polyclonal antibody specific for the mouse PARP1 acetylated at lysine 498 was generated (Abgenex Pvt. Ltd.). Briefly, rabbits were immunized with the acetylated mouse PARP1 peptide [PVEVVAPRGK(AcK)SGAALS]. Antisera from the immunized rabbits were affinity purified using the unacetylated peptide followed by the acetylated peptide. To detect various acetylated forms of PARP1, cell lysates were immunoprecipitated with PARP1 antibodies and then subjected to Western blotting with acetyl-specific antibodies. To detect PARylation, cell lysates were immunoprecipitated with PARP1 antibodies and then subjected to Western blotting with PAR-specific antibodies.

Immunoprecipitations were performed using 500 μg of cell extracts pre-treated with MNase, as previously described (*38*), and incubated with the indicated antibodies. Western blots were performed subsequently, as described earlier. For identifying PARP1 binding proteins, HT29 cells were infected with recombinant adenovirus expressing hemagglutinin (HA)-tagged PARP1^{K521Q} or PARP1^{K521R}. Twenty-four hours after infection, nuclear extracts were prepared. Precleared lysates were then immunoprecipitated with anti-HA antibody–conjugated agarose beads (Santa Cruz Biotechnology) and were eluted with HA peptide (Sigma-Aldrich). The eluate was resolved by SDS-PAGE and visualized by silver staining. The bands were excised and analyzed by mass spectrometry (ITSI Biosciences, USA).

In vitro deacetylation assay

An in vitro deacetylation assay was performed, as described previously (*39*). Briefly, in vitro deacetylation reactions were performed using human recombinant HDAC5 (Sigma-Aldrich) and acetylated PARP1 peptides (Sigma-Aldrich). The reaction mixture was run on an LC-MS/MS System (Thermo Fisher Scientific) and the data were analyzed by Proteome Discoverer software. Acetylated PARP1 peptides used in the assay are as follows: AcK498: VAPRGK(AcK)SGAAL, AcK505: SGAALSK(AcK)KSKG, AcK508: KSK(AcK)GQVKEEGIN, AcK521: NKSEK(AcK)RMKLTL, AcK524: RMK(AcK)LTLKGGAA.

Alkaline comet assay

A total of 1×10^3 cells/ml were mixed with 1% low melting point agarose, transferred onto slides, and allowed to settle. The slides were then immersed in lysis solution and subjected to electrophoresis as reported (*40*). Slides were stained with SYBR Gold (Invitrogen, USA). Imaging was done using a Zeiss ApoTome microscope and the images were analyzed with the OpenComet plugin for ImageJ software. In each experiment, 100 cells were scored per sample.

Proximity ligation assay

The PLA was performed using a Duolink in situ PLA kit (Sigma-Aldrich) according to the manufacturer's instructions. Slides were counterstained with 4′,6-diamidino-2-phenylindole (DAPI) Ultra-Cruz mounting medium (Santa Cruz Biotechnology). Imaging was done using a Zeiss ApoTome microscope and the images were analyzed with the ZEN Blue software. The following primary antibodies were used: HDAC5 (Santa Cruz Biotechnology), PARP1 (Santa Cruz Biotechnology), pADPr (Santa Cruz Biotechnology), Mre11 (Cell Signaling Technology), and ATF4 (Abcam).

Cell cycle analysis

BrdU (5-bromo-2-deoxyuridine) incorporation was measured as described previously (*41*). The cells were analyzed by flow cytometry using FACScan (BD Biosciences). Fluorescence-activated cell sorting (FACS) data were analyzed using Flowjo software.

RNA-seq and analysis

Total RNA was extracted using TRIzol reagent (Invitrogen) following the manufacturer's instructions. Transcriptome sequencing was performed on the Illumina platform (Neuberg Supratech, India). Quality assessment of the raw fastq reads of the sample was performed using FastQC v.0.11.9 (*42*). The processed reads were aligned to the STAR-indexed *Homo sapiens* (GRCh38) genome using STAR aligner v 2.7.9a. The differentially expressed genes were identified using DESeq2 (*43*).

Metabolite profiling

To determine metabolic profiles, metabolites were extracted and analyzed as described previously (*44*). Briefly, metabolites were extracted on dry ice with chilled 80% methanol. The extract was dried using a speed vacuum concentrator and resuspended in 80 ml of water. The samples were run on a Q-TOF Synapt G2 mass spectrometry (Waters) coupled to UPLC. MassLynx 4.1 software was used for data acquisition, data handling, and instrument control. MZmine 2 software was used for analysis. The relative quantification process was done by comparing the signal intensity or peak area of the specific metabolite relative to the control.

Quantification of Metabolites

For targeted quantification of specific intracellular metabolites, 2×10^5 cells were seeded in six-well plates for 24 hours before treatment and then treated with 5FU (Sigma-Aldrich) for indicated time points. The cells were harvested and suspended in phosphate-buffered saline (PBS). The kits used for the assays are described below. The amount of specific metabolite within a sample measured using kits was plotted relative to the control.

Glutamine quantification assay

The abundance of intracellular total Glutamine content was measured using a Glutamine Assay Kit (Elabscience) following the manufacturer's protocol and normalized to cell number. The Gln content was calculated by measuring the absorbance value at 450 nm.

Glutamate quantification assay

Total glutamate content was measured using a Glutamate Colorimetric/Fluorometric Assay Kit (Caymen Chemicals) as per the manufacturer's protocol and normalized to cell number. The absorbance was measured at 570 nm.

Alpha-ketoglutarate quantification assay

Total alpha-ketoglutarate content was measured using α-Ketoglutarate Assay Kit (Caymen Chemical) according to the manufacturer's protocol and normalized to cell number. The absorbance was measured at 570 nm.

Succinate quantification assay

Total succinate content was measured using EnzyChrom Succinate Assay Kit (Bioassay systems) according to the manufacturer's protocol and normalized to cell number. The absorbance was measured at 570 nm which correlates with the concentration of succinate in the sample.

Asparagine quantification assay

Total asparagine content was measured using the Asparagine Assay Kit (Abcam) according to the manufacturer's protocol and normalized to cell number. The fluorescence signal was measured at Ex/Em = 538/587 nm.

Arginine quantification assay

Total arginine content was measured using the Arginine Assay Kit (Abcam) according to the manufacturer's protocol and normalized to cell number. The colorimetric signal absorbance was measured at 450 nm.

Proline quantification assay

Total proline content was measured using Proline Assay Kit (Elabscience) according to the manufacturer's protocol and normalized to cell number. The concentration of proline can be calculated by measuring the absorbance at 520 nm.

Ornithine quantification assay

Total ornithine content was measured using Ornithine Assay Kit (Abcam) according to the manufacturer's protocol and normalized to cell number. The fluorescence signal was measured at Ex/Em = 538/587 nm.

Oxygen consumption rate measurement

OCR was determined using an XF24 flux analyzer (Seahorse Biosciences). OCR was analyzed under basal condition or in response to 5FU (Sigma-Aldrich) followed by injection with oligomycin, carbonyl cyanide *p*-trifluoromethoxyphenylhydrazone, and antimycin A, as described previously (*44*).

RT-qPCR

Total RNA extraction was carried out using TRIzol (Invitrogen). cDNA was synthesized using an iScript cDNA synthesis kit (Bio-Rad) as per the manufacturer's instruction. Quantitative polymerase chain reaction (qPCR) was carried out using Maxima SYBR Green Master Mix (Fermentas) in an Eppendorf real-time PCR machine. 18*S* ribosomal RNA served as internal control across all samples. ΔΔCt method was used for the analysis of the reverse transcription qPCR (RT-qPCR) data. Error bars are means ± SD of three independent experiments with triplicate samples. Primer sequences are listed in table S3.

ChIP assay

Chromatin immunoprecipitation (ChIP) was performed using a commercially available kit following the manufacturer's instructions (Millipore). Briefly, 1×10^7 cells were fixed with formaldehyde and lysed with SDS lysis buffer. The cell lysates were then subjected to sonication to fragment the DNA to lengths between 0.2 and 1 kb. The samples were precleared using Protein A Agarose/Salmon Sperm DNA slurry. Control immunoglobulin G (IgG) (Santa Cruz Biotechnology) or ATF4 (Santa Cruz Biotechnology) antibody was added and incubated overnight at 4°C. The samples were subsequently incubated with fresh Protein A Agarose/Salmon Sperm DNA slurry for 2 hours. The precipitated chromatin complexes were eluted by incubating the beads with 500 μl of elution buffer (1% SDS and 0.1 M $NaHCO_3$) for 30 min. Last, protein-DNA cross-links were reversed by heating at 65°C for 4 hours, and the immunoprecipitated DNA was analyzed by qPCR. For reChIP experiments, a part of the chromatin complexes immunoprecipitated with the anti-ATF4 antibody above was eluted by incubation for 30 min at 37°C in 100 μl of 10 mM dithiothreitol instead of elution buffer. Following centrifugation, the supernatant was diluted 20-fold with ChIP dilution buffer and re-immunoprecipitated with control IgG or PARP1 antibodies (Santa Cruz Biotechnology), and the ChIP protocol was repeated. Primers used for this analysis are provided in table S4.

Colony formation assay

Cells were counted and 1000 cells were seeded in a six-well culture dish. After 7 days of incubation, plates were gently washed with 1× PBS, fixed in methanol, and stained with 0.1% crystal violet. Colonies were manually counted.

Transwell migration assay

Cell migration was performed using the Cultrex cell migration assay kit (Trevigen), following the manufacturer's instructions. Briefly, 1×10^5 cells were seeded in serum-free DMEM in the upper chamber of a 24-well Transwell plate, while the lower chamber contained DMEM medium with 10% (v/v) FBS. After 24 hours, the cells were collected in a cell dissociation solution containing 1 μM of calcein-AM. The plate was read using 485-nm excitation and 520-nm emission filters, and percentages of migrated cells were calculated from the standard curve established for respective cell lines.

Transwell invasion assay

Cell invasion through basement membranes was assayed using the Cultrex Coat BME-coated cell invasion assay (Trevigen), as per the manufacturer's instructions. At first, rehydration of the membranes was performed, and then the protocol described in the migration assay above was followed.

Xenograft studies

All the animal studies were approved by the Institutional Animal Care and Use Committee of the National Institute of Immunology, New Delhi, India. Female nude mice (nu/nu) were subcutaneously injected with 4×10^6 cells/0.1 ml of DMEM. After 1 week of injection, 5FU was injected intraperitoneally at a dose of 25 mg/kg per mouse every alternate day. Mice were injected intraperitoneally with olaparib (Sigma-Aldrich) at a dose of 10 mg/kg daily or talazoparib (Sigma-Aldrich) at a dose of 2 mg/kg daily. Tumor volume (in cubic millimeters) was measured with a slide caliper and calculated using the formula: (widest diameter × smallest diameter^2)/2. At the end of the experiment, the mice were euthanized and the tumors were harvested. Tumor extracts were then prepared, followed by immunoblotting as described earlier. For immunohistochemical analysis, tumors were fixed in formalin, washed with PBS, and embedded in paraffin for sectioning. Five-millimeter sections were dewaxed and immunostained with Ki67 (Santa Cruz Biotechnology, sc-23900), CD31 (Santa Cruz Biotechnology, sc-376764), and γH2AX (Abcam, ab11174) antibody. For secondary detection, anti-mouse Alexa Fluor 555 (Molecular Probes) and anti-rabbit Alexa Fluor 546 (Molecular Probes) antibodies were used. TUNEL staining was performed using the TUNEL Assay Kit (Promega) as per the manufacturer's protocol. Sections were counterstained using DAPI. Imaging was done using a Zeiss ApoTome microscope and the images were analyzed with the ZEN Blue software.

In vivo metastasis assay

HT29 cells were stably transfected (pooled neomycin-resistant population) with pGL4.51[*luc2*/CMV/Neo] plasmid (Promega) to generate HT29^{Luc2} cells. The cell suspension was injected orthotopically into the cecum wall of female nude mice. After 1 week of injection, 5FU was injected intraperitoneally at a dose of 25 mg/kg per mouse every alternate day. Mice were injected intraperitoneally with olaparib at a dose of 10 mg/kg daily for 4 weeks. For weekly in vivo bioluminescence imaging, the mice were anesthetized using ketamine (80 mg/kg) and xylazine (10 mg/kg) by intraperitoneal injection. The anesthetized mice were administered D-luciferin (150 mg/kg) in PBS intraperitoneally. Imaging was performed using the Spectral LAGO X imaging system, and image analysis was performed using Aura imaging software. At the end of the experiment, the mice were euthanized. The liver and lung were excised and ex vivo imaging was performed. Primary tumors were excised and Western blot analysis was performed as described earlier. Hematoxylin and eosin staining was performed, as described previously (*45*). Genomic DNA was isolated from blood obtained from euthanized mice for measurement of circulating tumor cells using the DNeasy Blood and Tissue Kit (Qiagen). qPCR was performed using primers specific to the human *Alu* repeat sequence (Fwd 5′-ACGCCTGTAATCCCAGCACTT-3′; Rev. 5′-TCGCCCAGGCTGGAGTGC-3′), while mouse *actin* served as the control (Fwd 5′-GCTTCTTTGCAGCTCCTTCGTTG-3′; Rev. 5′-TTTGCACATGCCGGAGCCGTTGT-3′).

Tissue microarray

Human colon adenocarcinoma and matched normal adjacent tissue sections were procured from US Biomax as tissue microarrays. Immunofluorescence was performed as described previously (*45*). Briefly, the paraffin sections were dewaxed and incubated with HDAC5 (Santa Cruz Biotechnology, Sc-133106), AcK498-PARP1, and AcK521-PARP1 antibodies (CSB-PA890185). Anti-mouse Alexa Fluor 488 (Molecular Probes, A11001), anti-rabbit Alexa Fluor 555 antibody (Molecular Probes, A21428), and anti-rabbit Alexa 546 (Molecular Probes) were used for secondary detection. Slides were mounted with ProLong Gold antifade reagent with DAPI (Molecular Probes) and imaging was performed using a Zeiss Apotome microscope. The images were analyzed using Zeiss ZEN Blue software and ImageJ software was used for quantitation. The average signal intensity (in arbitrary units, AU) from four random fields was used for the analysis.

Statistical analysis

All experiments were conducted independently at least three times. Results were expressed as means ± SD. The sample size was chosen to give sufficient power for calling significance with standard statistical tests. Statistical analyses were performed by a standard two-tailed Student's *t* test or one-way analysis of variance (ANOVA). $***P < 0.005$ was considered significant.

Supplementary Materials

This PDF file includes:

Figs. S1 to S13
Tables S1 to S4

REFERENCES AND NOTES

1. A. Ray Chaudhuri, A. Nussenzweig, The multifaceted roles of PARP1 in DNA repair and chromatin remodelling. *Nat. Rev. Mol. Cell Biol.* **18**, 610–621 (2017).
2. A. A. E. Ali, G. Timinszky, R. Arribas-Bosacoma, M. Kozlowski, P. O. Hassa, M. Hassler, A. G. Ladurner, L. H. Pearl, A. W. Oliver, The zinc-finger domains of PARP1 cooperate to recognize DNA strand breaks. *Nat. Struct. Mol. Biol.* **19**, 685–692 (2012).
3. J. F. Haince, D. McDonald, A. Rodrigue, U. Déry, J. Y. Masson, M. J. Hendzel, G. G. Poirier, PARP1-dependent kinetics of recruitment of MRE11 and NBS1 proteins to multiple DNA damage sites. *J. Biol. Chem.* **283**, 1197–1208 (2008).
4. W. Zong, Y. Gong, W. Sun, T. Li, Z. Q. Wang, PARP1: Liaison of chromatin remodeling and transcription. *Cancers* **14**, 4162 (2022).
5. M. J. Schiewer, K. E. Knudsen, Transcriptional roles of PARP1 in cancer. *Mol. Cancer Res.* **12**, 1069–1080 (2014).
6. T. A. McKinsey, C. L. Zhang, E. N. Olson, Activation of the myocyte enhancer factor-2 transcription factor by calcium/calmodulin-dependent protein kinase-stimulated binding of 14-3-3 to histone deacetylase 5. *Proc. Natl. Acad. Sci. U.S.A.* **97**, 14400–14405 (2000).
7. C. H. Ha, J. Y. Kim, J. Zhao, W. Wang, B. S. Jhun, C. Wong, Z. G. Jin, PKA phosphorylates histone deacetylase 5 and prevents its nuclear export, leading to the inhibition of gene transcription and cardiomyocyte hypertrophy. *Proc. Natl. Acad. Sci. U.S.A.* **107**, 15467–15472 (2010).

8. H. Li, H. Xie, W. Liu, R. Hu, B. Huang, Y. F. Tan, E. Y. Liao, K. Xu, Z. F. Sheng, H. D. Zhou, X. P. Wu, X. H. Luo, A novel microRNA targeting HDAC5 regulates osteoblast differentiation in mice and contributes to primary osteoporosis in humans. *J. Clin. Invest.* **119**, 3666–3677 (2009).
9. G. Li, Y. Tian, W. G. Zhu, The roles of histone deacetylases and their inhibitors in cancer therapy. *Front. Cell Dev. Biol.* **8**, 576946 (2020).
10. L. Zhong, S. Sun, S. Yao, X. Han, M. Gu, J. Shi, Histone deacetylase 5 promotes the proliferation and invasion of lung cancer cells. *Oncol. Rep.* **40**, 2224–2232 (2018).
11. J. Liu, J. Gu, Z. Feng, Y. Yang, N. Zhu, W. Lu, F. Qi, Both HDAC5 and HDAC6 are required for the proliferation and metastasis of melanoma cells. *J. Transl. Med.* **14**, 7 (2016).
12. S. Feng, L. Zhang, X. Liu, G. Li, B. Zhang, Z. Wang, H. Zhang, H. Ma, Low levels of AMPK promote epithelial-mesenchymal transition in lung cancer primarily through HDAC4- and HDAC5-mediated metabolic reprogramming. *J. Cell. Mol. Med.* **24**, 7789–7801 (2020).
13. J. Yang, C. Gong, Q. Ke, Z. Fang, X. Chen, M. Ye, X. Xu, Insights into the function and clinical application of HDAC5 in cancer management. *Front. Oncol.* **11**, 661620 (2021).
14. N. Sen, R. Kumari, M. I. Singh, S. Das, HDAC5, a key component in temporal regulation of p53-mediated transactivation in response to genotoxic stress. *Mol. Cell* **52**, 406–420 (2013).
15. P. O. Hassa, S. S. Haenni, C. Buerki, N. I. Meier, W. S. Lane, H. Owen, M. Gersbach, R. Imhof, M. O. Hottiger, Acetylation of poly(ADP-ribose) polymerase-1 by p300/CREB-binding protein regulates coactivation of NF-kappaB-dependent transcription. *J. Biol. Chem.* **280**, 40450–40464 (2005).
16. M. Ghandi, F. W. Huang, J. Jané-Valbuena, G. V. Kryukov, C. C. Lo, E. R. McDonald III, J. Barretina, E. T. Gelfand, C. M. Bielski, H. Li, K. Hu, A. Y. Andreev-Drakhlin, J. Kim, J. M. Hess, B. J. Haas, F. Aguet, B. A. Weir, M. V. Rothberg, B. R. Paolella, M. S. Lawrence, R. Akbani, Y. Lu, H. L. Tiv, P. C. Gokhale, A. de Weck, A. A. Mansour, C. Oh, J. Shih, K. Hadi, Y. Rosen, J. Bistline, K. Venkatesan, A. Reddy, D. Sonkin, M. Liu, J. Lehar, J. M. Korn, D. A. Porter, M. D. Jones, J. Golji, G. Caponigro, J. E. Taylor, C. M. Dunning, A. L. Creech, A. C. Warren, J. M. McFarland, M. Zamanighomi, A. Kauffmann, N. Stransky, M. Imielinski, Y. E. Maruvka, A. D. Cherniack, A. Tsherniak, F. Vazquez, J. D. Jaffe, A. A. Lane, D. M. Weinstock, C. M. Johannessen, M. P. Morrissey, F. Stegmeier, R. Schlegel, W. C. Hahn, G. Getz, G. B. Mills, J. S. Boehm, T. R. Golub, L. A. Garraway, W. R. Sellers, Next-generation characterization of the cancer cell line encyclopedia. *Nature* **569**, 503–508 (2019).
17. K. C. G. Berg, P. W. Eide, I. A. Eilertsen, B. Johannessen, J. Bruun, S. A. Danielsen, M. Bjørnslett, L. A. Meza-Zepeda, M. Eknæs, G. E. Lind, O. Myklebost, R. I. Skotheim, A. Sveen, R. A. Lothe, Multi-omics of 34 colorectal cancer cell lines—A resource for biomedical studies. *Mol. Cancer* **16**, 116 (2017).
18. G. Liszczak, K. L. Diehl, G. P. Dann, T. W. Muir, Acetylation blocks DNA damage-induced chromatin ADP-ribosylation. *Nat. Chem. Biol.* **14**, 837–840 (2018).
19. J. Murai, S. Y. N. Huang, B. B. das, A. Renaud, Y. Zhang, J. H. Doroshow, J. Ji, S. Takeda, Y. Pommier, Trapping of PARP1 and PARP2 by clinical PARP inhibitors. *Cancer Res.* **72**, 5588–5599 (2012).
20. G. Reginato, P. Cejka, The MRE11 complex: A versatile toolkit for the repair of broken DNA. *DNA Repair* **91-92**, 102869 (2020).
21. M. Tanabe, H. Izumi, T. Ise, S. Higuchi, T. Yamori, K. Yasumoto, K. Kohno, Activating transcription factor 4 increases the cisplatin resistance of human cancer cell lines. *Cancer Res.* **63**, 8592–8595 (2003).
22. I. M. N. Wortel, L. T. van der Meer, M. S. Kilberg, F. N. van Leeuwen, Surviving stress: Modulation of ATF4-mediated stress responses in normal and malignant cells. *Trends Endocrinal. Metal.* **28**, 794–806 (2017).
23. J. Jin, J. K. Byun, Y. K. Choi, K. G. Park, Targeting glutamine metabolism as a therapeutic strategy for cancer. *Exp. Mol. Med.* **55**, 706–715 (2023).
24. N. J. Curtin, C. Szabo, Poly(ADP-ribose) polymerase inhibition: Past, present and future. *Nat. Rev. Drug Discov.* **19**, 711–736 (2020).
25. Q. Liu, Y. Sun, J. M. Zheng, X. L. Yan, H. M. Chen, J. K. Chen, H. Q. Huang, Formononetin sensitizes glioma cells to doxorubicin through preventing EMT via inhibition of histone deacetylase 5. *Int. J. Clin. Exp. Pathol.* **8**, 6434–6441 (2015).
26. Z. Mao, C. Hine, X. Tian, M. van Meter, M. Au, A. Vaidya, A. Seluanov, V. Gorbunova, SIRT6 promotes DNA repair under stress by activating PARP1. *Science* **332**, 1443–1446 (2011).
27. C. Robert, P. K. Nagaria, N. Pawar, A. Adewuyi, I. Gojo, D. J. Meyers, P. A. Cole, F. V. Rassool, Histone deacetylase inhibitors decrease NHEJ both by acetylation of repair factors and trapping of PARP1 at DNA double-strand breaks in chromatin. *Leuk. Res.* **45**, 14–23 (2016).
28. P. O. Hassa, M. O. Hottiger, A role of poly (ADP-ribose) polymerase in NF-kappaB transcriptional activation. *Biol. Chem.* **380**, 953–959 (1999).
29. D. Martin-Oliva, F. O'Valle, J. A. Muñoz-Gámez, M. T. Valenzuela, M. I. Nuñez, M. Aguilar, J. M. R. de Almodóvar, R. G. del Moral, F. J. Oliver, Crosstalk between PARP-1 and NF-kappaB modulates the promotion of skin neoplasia. *Oncogene* **23**, 5275–5283 (2004).
30. M. Elser, L. Borsig, P. O. Hassa, S. Erener, S. Messner, T. Valovka, S. Keller, M. Gassmann, M. O. Hottiger, Poly(ADP-ribose) polymerase 1 promotes tumor cell survival by coactivating hypoxia-inducible factor-1-dependent gene expression. *Mol. Cancer Res.* **6**, 282–290 (2008).
31. M. M. Murata, X. Kong, E. Moncada, Y. Chen, H. Imamura, P. Wang, M. W. Berns, K. Yokomori, M. A. Digman, NAD+ consumption by PARP1 in response to DNA damage triggers metabolic shift critical for damaged cell survival. *Mol. Biol. Cell* **30**, 2584–2597 (2019).
32. L. Geng, M. Zhu, D. Luo, H. Chen, B. Li, Y. Lao, H. An, Y. Wu, Y. Li, A. Xia, Y. Shi, Z. Tong, S. Lu, D. Xu, X. Wang, W. Zhang, B. Sun, Z. Xu, TKT-PARP1 axis induces radioresistance by promoting DNA double-strand break repair in hepatocellular carcinoma. *Oncogene* **43**, 682–692 (2024).
33. K. Huang, M. du, X. Tan, L. Yang, X. Li, Y. Jiang, C. Wang, F. Zhang, F. Zhu, M. Cheng, Q. Yang, L. Yu, L. Wang, D. Huang, K. Huang, PARP1-mediated PPARalpha poly(ADP-ribosyl)ation suppresses fatty acid oxidation in non-alcoholic fatty liver disease. *J. Hepatol.* **66**, 962–977 (2017).
34. D. R. Wise, C. B. Thompson, Glutamine addiction: A new therapeutic target in cancer. *Trends Biochem. Sci.* **35**, 427–433 (2010).
35. Y. K. Satija, S. Das, Tyr99 phosphorylation determines the regulatory milieu of tumor suppressor p73. *Oncogene* **35**, 513–527 (2016).
36. T. C. He, S. Zhou, L. T. da Costa, J. Yu, K. W. Kinzler, B. Vogelstein, A simplified system for generating recombinant adenoviruses. *Proc. Natl. Acad. Sci. U.S.A.* **95**, 2509–2514 (1998).
37. C. M. Dowling, K. E. R. Hollinshead, A. di Grande, J. Pritchard, H. Zhang, E. T. Dillon, K. Haley, E. Papadopoulos, A. K. Mehta, R. Bleach, A. U. Lindner, B. Mooney, H. Düssmann, D. O'Connor, J. H. M. Prehn, K. Wynne, M. Hemann, J. E. Bradner, A. C. Kimmelman, J. L. Guerriero, G. Cagney, K. K. Wong, A. G. Letai, T. N. Chonghaile, Multiple screening approaches reveal HDAC6 as a novel regulator of glycolytic metabolism in triple-negative breast cancer. *Sci. Adv.* **7**, eabc4897 (2021).
38. S. Sharma, W. Tyagi, R. Tamang, S. Das, HDAC5 modulates SATB1 transcriptional activity to promote lung adenocarcinoma. *Br. J. Cancer* **129**, 586–600 (2023).
39. E. Michishita, R. A. McCord, E. Berber, M. Kioi, H. Padilla-Nash, M. Damian, P. Cheung, R. Kusumoto, T. L. A. Kawahara, J. C. Barrett, H. Y. Chang, V. A. Bohr, T. Ried, O. Gozani, K. F. Chua, SIRT6 is a histone H3 lysine 9 deacetylase that modulates telomeric chromatin. *Nature* **452**, 492–496 (2008).
40. P. L. Olive, J. P. Banath, The comet assay: A method to measure DNA damage in individual cells. *Nat. Protoc.* **1**, 23–29 (2006).
41. S. Das, W. S. El-Deiry, K. Somasundaram, Regulation of the p53 homolog p73 by adenoviral oncogene E1A. *J. Biol. Chem.* **278**, 18313–18320 (2003).
42. A. Dobin, C. A. Davis, F. Schlesinger, J. Drenkow, C. Zaleski, S. Jha, P. Batut, M. Chaisson, T. R. Gingeras, STAR: Ultrafast universal RNA-seq aligner. *Bioinformatics* **29**, 15–21 (2013).
43. M. I. Love, W. Huber, S. Anders, Moderated estimation of fold change and dispersion for RNA-seq data with DESeq2. *Genome Biol.* **15**, 550 (2014).
44. G. Eelen, C. Dubois, A. R. Cantelmo, J. Goveia, U. Brüning, M. DeRan, G. Jarugumilli, J. van Rijssel, G. Saladino, F. Comitani, A. Zecchin, S. Rocha, R. Chen, H. Huang, S. Vandekeere, J. Kalucka, C. Lange, F. Morales-Rodriguez, B. Cruys, L. Treps, L. Ramer, S. Vinckier, K. Brepoels, S. Wyns, J. Souffreau, L. Schoonjans, W. H. Lamers, Y. Wu, J. Haustraete, J. Hofkens, S. Liekens, R. Cubbon, B. Ghesquière, M. Dewerchin, F. L. Gervasio, X. Li, J. D. van Buul, X. Wu, P. Carmeliet, Role of glutamine synthetase in angiogenesis beyond glutamine synthesis. *Nature* **561**, 63–69 (2018).
45. M. Ghosh, S. Das, PRAMEF2-mediated dynamic regulation of YAP signaling promotes tumorigenesis. *Proc. Natl. Acad. Sci. U.S.A.* **118**, e2105523118 (2021).

Acknowledgments: We thank the members of the Molecular Oncology Laboratory for helpful discussions. W.T. was supported by a fellowship from the Department of Science & Technology, Government of India. BioRender.com was used to create schematics in the figures. **Funding:** This work was supported by a grant from the Science and Engineering Research Board, Government of India (CRG/2021/000603/IBS) to S.D. The authors also acknowledge the financial support from the NII Core Fund. **Author contributions:** Conceptualization: W.T. and S.D. Methodology: W.T. and S.D. Experiment design: W.T. and S.D. Investigation: W.T. and S.D. Visualization: W.T. and S.D. Supervision: W.T. and S.D. Writing—original draft: W.T. and S.D. Writing—review and editing: W.T. and S.D. **Competing interests:** The authors declare that they have no competing interests. **Data and materials availability:** All data needed to evaluate the conclusions in the paper are present in the paper and/or the Supplementary Materials. The RNA sequencing data have been deposited in the Gene Expression Omnibus (GEO) of NCBI under the accession number GSE269944.

Submitted 21 February 2024
Accepted 13 September 2024
Published 18 October 2024
10.1126/sciadv.ado7720